Monthly Notices
of the
ROYAL ASTRONOMICAL SOCIETY

Mon. Not. R. Astron. Soc. **418,** 888–905 (2011) doi:10.1111/j.1365-2966.2011.19542.x

Galactic foreground contributions to the 5-year *Wilkinson Microwave Anisotropy Probe* maps

N. Macellari,[1] E. Pierpaoli,[1] C. Dickinson[2⋆] and J. E. Vaillancourt[3]†

[1]*University of Southern California, Los Angeles, CA 90089-0484, USA*
[2]*Jodrell Bank Centre for Astrophysics, Alan Turing Building, School of Physics & Astronomy, University of Manchester, Oxford Road, Manchester M13 9PL*
[3]*Division of Physics, Mathematics & Astronomy, California Institute of Technology, 1200 East California Boulevard, Pasadena, CA 91125, USA*

Accepted 2011 July 28. Received 2011 July 12; in original form 2009 December 23

ABSTRACT

We compute the cross-correlation between intensity and polarization from the 5-year *Wilkinson Microwave Anisotropy Probe* (*WMAP*5) data in different sky regions with respect to template maps for synchrotron, dust and free–free emission. We derive the frequency dependence and polarization fraction for all three components in 48 different sky regions of HEALPix ($N_{\rm side} = 2$) pixelization. The anomalous emission associated with dust is clearly detected in intensity over the entire sky at the *K* (23-GHz) and *Ka* (33-GHz) *WMAP* bands, and is found to be the dominant foreground at low Galactic latitudes, between $b = -40^\circ$ and $+10^\circ$. The synchrotron spectral index obtained from the *K* and *Ka WMAP* bands from an all-sky analysis is $\beta_{\rm s} = -3.32 \pm 0.12$ for intensity and $\beta_{\rm s} = -3.01 \pm 0.03$ for polarized intensity.

The polarization fraction of the synchrotron emission is constant in frequency and increases with latitude from ≈5 per cent near the Galactic plane up to ≈40 per cent in some regions at high latitudes; the average value for $|b| < 20^\circ$ is $8.6 \pm 1.7\,({\rm stat}) \pm 0.5\,({\rm sys})$ per cent, while for $|b| > 20^\circ$, it is $19.3 \pm 0.8\,({\rm stat}) \pm 0.5\,({\rm sys})$ per cent. Anomalous dust and free–free emissions appear to be relatively unpolarized. Monte Carlo simulations showed that there were biases of the method due to cross-talk between the components, at up to ≈5 per cent in any given pixel, and ≈1.5 per cent on average, when the true polarization fraction is low (a few per cent or less). Nevertheless, the average polarization fraction of dust-correlated emission at the *K* band is $3.2 \pm 0.9\,({\rm stat}) \pm 1.5\,({\rm sys})$ per cent or less than 5 per cent at 95 per cent confidence. When comparing real data with simulations, eight regions show a detected polarization above the 99th percentile of the distribution from simulations with no input foreground polarization, six of which are detected at above 2σ and display polarization fractions between 2.6 and 7.2 per cent, except for one anomalous region, which has 32 ± 12 per cent. The dust polarization values are consistent with the expectation from spinning dust emission, but polarized dust emission from magnetic-dipole radiation cannot be ruled out. Free–free emission was found to be unpolarized with an upper limit of 3.4 per cent at 95 per cent confidence.

Key words: polarization – ISM: general – Galaxy: general – cosmic background radiation – diffuse radiation – radio continuum: ISM.

1 INTRODUCTION

During the last few years, great advances have been made in measuring the cosmic microwave background (CMB) anisotropies. More advances are expected from the *Planck* mission that will provide all-sky temperature and polarization CMB measurements with high accuracy and unprecedented frequency coverage. As CMB experiments reach higher sensitivity, it becomes necessary to better understand and remove the contribution from competing Galactic and extragalactic astrophysical signals in the same frequency bands. It is well known that the emission of these foregrounds rivals the temperature signal over a significant fraction of the sky and dominates the polarization signal over most of the sky (Kogut et al. 2007). As the temperature power spectrum has already been measured with great precision (e.g. VSA, Dickinson et al. 2004; Boomerang, Jones et al. 2006; *Wilkinson Microwave Anisotropy Probe*, hereinafter *WMAP*5,

⋆E-mail: Clive.Dickinson@manchester.ac.uk
†Present address: Stratopsheric Observatory for Infrared Astronomy, Universities Space Research Association, NASA Ames Research Center, Moffett Field, CA 94035-1000, USA.

Nolta et al. 2009; QUaD, Pryke et al. 2009; ACBAR, Reichardt et al. 2009; CBI, Sievers et al. 2009), most observations are now concentrating on polarization measurements (e.g. QUaD, Brown et al. 2009; BICEP, Chiang et al. 2010). For the study of polarization anisotropies, however, foregrounds may be the limiting factor, as the primordial signal is much weaker than intensity while the foregrounds are not well characterized at the relevant frequencies at this time. For this reason, suitable component-separation techniques have been developed and are being applied to current data (Kogut et al. 2007; Eriksen et al. 2008; Delabrouille & Cardoso 2009; Dunkley et al. 2009; Gold et al. 2009), in preparation for *Planck* data and future satellite missions (Leach et al. 2008; Betoule et al. 2009). In some instances, such techniques rely on prior information acquired on the emission of a specific foreground, for which a prior characterization is necessary. Moreover, the study of foregrounds in the microwave band is of astrophysical interest on its own, as it can be informative about physical phenomena occurring in our Galaxy and in others.

Foregrounds are either Galactic or extragalactic in nature. In this paper, we are interested in the Galactic emission, which dominates over extragalactic emission at intermediate to large scales ($\gtrsim 1^\circ$). The Galactic emission has three main components: dust, synchrotron and free–free, of which only dust and synchrotron are expected to show significant polarization. In contrast with extragalactic emission, we do not expect the Galactic foreground to be isotropic. For this reason, Galactic foregrounds need a characterization that is both scale-dependent and position-dependent.

The most common methods for extracting foreground information from CMB data involve fitting a given theoretical model to the data. These fitting procedures typically assume that a specific foreground follows a power law in frequency and is characterized by a given polarization fraction and a (fixed) angle. For instance, this is the approach of the *WMAP* teams [Kogut et al. (2007) for the *WMAP*3 and Gold et al. (2009) for the *WMAP*5 data].

By so doing, however, the diverse behaviour of different foregrounds in different regions of the sky may be neglected. For instance, a spinning dust contribution may not have a power-law frequency dependence, and may make different contributions in different areas of the sky. A variety of dust grains may populate different areas of our Galaxy, and have different contributions to the intensity and polarization signal at the observed frequencies. The synchrotron emission clearly depends on the energy spectrum of electrons in a given region, while the polarization signal may be affected by depolarization effects which are more severe in denser or less uniform regions.

In this paper, we aim to characterize the contribution of the three Galactic components in the microwave band in temperature and polarization by studying the *WMAP*5 data (Hinshaw et al. 2009; Nolta et al. 2009), including their frequency and spatial dependencies. To achieve this goal, we develop a foreground analysis that assumes no frequency model and only relies on a morphological characterization of foregrounds as derived at non-CMB frequencies. Specifically, we use a cross-correlation (C-C) analysis with standard foreground templates. Such an analysis method has been widely used by other authors studying CMB intensity data (e.g. de Oliveira-Costa et al. 1999, 2002; Banday et al. 2003; Bennett et al. 2003; Davies et al. 2006), but has not been applied to polarization data. An advantage of using such a method is the possibility of detecting particular emission processes associated with one of the three foreground templates even if its frequency and/or polarization characteristics are unknown. For example, this may be true in the case of a spinning dust component.

A possible limitation of the C-C method is that it allows characterization of only foreground components whose spatial distribution is well traced by the templates. These templates were derived at very different frequencies from the CMB measurements, and may not fully represent the morphology of a particular component in the range of frequencies at hand. Most analyses of *WMAP*5 polarization data are based on modelling the various emission components in the Q and U maps; here, we will perform our analysis in the polarization intensity P. This choice avoids the problem of modelling the Galactic magnetic field to compute the polarization angle, or of assuming a specific polarization angle as a function of position for each component. Under the hypothesis that all components have the same polarization angle (even if possibly a different polarization intensity), the method used in analysing the temperature maps can be readily extended to the polarization maps. Although a more general approach may be sought, as both dust grains' orientation and synchrotron emission are dictated by the direction of the magnetic field, this assumption may not be unreasonable.

Section 2 describes the *WMAP* data used in this work and the choices made about spatial resolution and masking, while Section 3 gives an introduction to the various sources of foreground emission and the spatial templates that will be used to trace each component. The C-C analysis technique and the computation of uncertainties are discussed in Section 4. The results of the analysis in both temperature and polarization are presented in Section 5, along with separate discussions for each of the three emission components. The main conclusions are summarized in Section 6.

2 *WMAP* DATA

We use the *WMAP*5 data (Hinshaw et al. 2009), consisting of five full-sky maps at frequencies of 22.8 GHz (K band), 33.0 GHz (Ka band), 40.7 GHz (Q band), 60.8 GHz (V band) and 93.5 GHz (W band), as provided on the Legacy Archive for Microwave Background Data Analysis (LAMBDA) website.[1] These maps are provided in HEALPix[2] format at a resolution of $N_{\rm side} = 512$ (number of pixels on the sphere $= 12 \times N_{\rm side}^2$). The maps are then downgraded to a HEALPix resolution of $N_{\rm side} = 32$, using the ud_grade[3] HEALPix routine, to give a total of 12 288 pixels. We chose this resolution as a compromise between obtaining a reasonable signal-to-noise ratio (S/N) and having small enough pixels to keep the information about foreground variations needed in the C-C analysis; with $N_{\rm side} = 16$, the resolution is becoming too coarse. Larger pixels are also likely to invalidate the assumption of a constant polarization fraction. Parallel transport of polarization vectors on the sphere is not considered in the averaging since the effect is at the 10^{-4} level or lower.

We convert the data from thermodynamic temperature to brightness (antenna) temperature using the conversion formula

$$T_{\rm A} = \frac{x^2 {\rm e}^x}{({\rm e}^x - 1)^2} T_{\rm CMB}, \quad (1)$$

where $x \equiv (h\nu)/(kT_0)$, T_0 being the CMB temperature of 2.725 K (Mather et al. 1999); this corresponds to a correction of 1 per cent at the K band and 25 per cent at the$W$ band.

We apply the *WMAP* team mask KQ85 (Gold et al. 2009) to the *WMAP* maps, in order to avoid the Galactic plane and bright point sources. The mask is provided in a $N_{\rm side} = 512$ HEALPix

[1] http://lambda.gsfc.nasa.gov/

[2] http://www.eso.org/science/healpix/ (Górski et al. 2005)

[3] Simple averaging is used, rather than a noise-weighted average.

resolution, so we downgrade it to our working resolution ($N_{\rm side} = 32$) and consider in the analysis only the coarse pixels that are completely outside the $N_{\rm side} = 512$ masked region. This procedure reduces to 8099 the number of data pixels (66 per cent of the sky) used in the analysis.

In the polarization analysis, we compute the total polarization as $P = \sqrt{Q^2 + U^2}$. The mask and the resolution chosen are the same as the intensity analysis. This allows direct comparison of the C-C coefficients fit for the temperature and polarization data, and calculation of the fractional polarization at the same sky positions.

3 GALACTIC COMPONENTS' EMISSION AND TEMPLATES

3.1 Synchrotron

Synchrotron emission arises from accelerating cosmic-ray electrons spiralling in the Galactic magnetic field. The emission depends on the energy spectrum of the electrons and on the intensity of the magnetic field, which results in significant spatial variations in spectral index on the sky. The synchrotron spectrum is approximated by a power law $T \sim \nu^{\beta_{\rm s}}$, typically with $\beta_{\rm s} \approx -2.7$ at radio wavelengths, steepening to $\beta_{\rm s} \approx -3.0$ at *WMAP* frequencies and with typical spatial variations of ± 0.2. Moreover, it is known that a pure synchrotron spectrum steepens with frequency due to the effects of spectral ageing, although in reality, a flattening of the spectrum can occur due to the presence of multiple components (e.g. Kogut et al. 2007).

Most of the information we have for synchrotron emission comes from low-frequency radio surveys, where synchrotron emission dominates the sky. In particular, large-area radio surveys at 408 MHz (Haslam et al. 1981, 1982), 1420 MHz (Reich & Reich 1986) and 2.3 GHz (Jonas, Baart & Nicolson 1998) give us a clear picture of the synchrotron component and these have been used extensively for foreground subtraction and previous C-C studies. The drawbacks of using such templates are: (i) there is a large extrapolation in frequency from ∼1 GHz to *WMAP* frequencies that is likely to result in some distortion of the morphology; (ii) baseline (offset) issues result in striping in the maps; and (iii) discrete extragalactic sources contaminate the diffuse emission. Several efforts have been made to reduce the effects of striping and source contamination (e.g. Davies, Watson & Gutierrez 1996; Platania et al. 2003) including the NCSA version of the Haslam et al. 408-MHz map, available on the LAMBDA website. We use this as our template for synchrotron emission.

Synchrotron emission is, by nature, highly polarized. For a power-law distribution of electron energies, $N(E) \propto E^{-p}$, propagating in a uniform magnetic field, the resulting emission is polarized with fractional linear polarization $f_{\rm s} = (p + 1)/(p + 7/3)$ aligned perpendicular to the magnetic field (Rybicki & Lightman 1979). The frequency dependence of synchrotron emission is also related to the electron energy distribution, $T(\nu) \propto \nu^{\beta_{\rm s}}$ with spectral index $\beta_{\rm s} = -(p + 3)/2$. For $\beta_{\rm s} \approx -3$, the synchrotron emission can have a maximum fractional polarization as high as $f_{\rm s} = 0.75$. However, line-of-sight and beam averaging effects will tend to reduce this, with typical values at high latitudes of ∼10–40 per cent.

3.2 Dust

The Galactic foreground at far-infrared and submillimetre wavelengths ($\nu \gtrsim 100$ GHz) is dominated by the thermal emission from warm ($T \sim 10$–100 K) interstellar dust grains. The intensity spectrum peaks in the range 100–200 μm and is well modelled by an emissivity-modified greybody of the form $\nu^{\beta_{\rm d}} B_\nu(T)$, where $B_\nu(T)$ is the Planck function at frequency ν and temperature T. Using data at 100 and 240 μm, Finkbeiner, Davis & Schlegel (1999) modelled the all-sky emission with two components having mean temperatures of 9.4 and 16 K and spectral indices of $\beta_{\rm d} = 1.7$ and 2.7, respectively. The predictions at longer wavelengths are in good agreement with observations at 353 GHz by *Archeops* (Ponthieu et al. 2005) and at 94 GHz by the *WMAP* (Bennett et al. 2003). We use the predictions at 94 GHz, which are available on the LAMBDA website, as our template for dust emission.

Polarization from thermally emitting dust is due to aspherical grains whose spin-axes have become aligned locally with interstellar magnetic fields (e.g. see reviews by Lazarian 2003, 2007). The most efficient direction for emission and absorption/extinction is the long grain-axis (perpendicular to the spin-axis). The observed polarization direction is then perpendicular to the aligning magnetic field in the case of grain emission, but parallel to the field in the case of background-starlight extinction. The expected size of the polarization depends on a number of unknown factors including the efficiency of the alignment mechanism and the inclination of the magnetic field to the line of sight. Typical background-starlight polarization has values in the ∼1–4 per cent range (e.g. Heiles 2000; Fosalba et al. 2002), while polarized emission in dense Galactic clouds has been observed at 0.5–10 per cent (e.g. Dotson et al. 2000, 2010; Matthews et al. 2009). *WMAP* polarization observations at 94 GHz (Kogut et al. 2007; Page et al. 2007) and *Archeops* observations at 353 GHz (Ponthieu et al. 2005) measure dust polarizations of ∼1 per cent in the Galactic plane, increasing to a few per cent at higher latitudes. Studies of the frequency dependence of polarized emission have found that the spectrum has a polarization minimum at $\lambda \sim 350$ μm, increasing to longer wavelengths (e.g. Hildebrand et al. 1999; Vaillancourt et al. 2008). However, these studies are limited to $\lambda = 60$–1300 μm and to bright/dense Galactic clouds. Extrapolating this spectrum to the conditions expected to prevail in the high-latitude diffuse interstellar medium (ISM), one expects a more featureless spectrum for wavelengths a few times longer than about 1 mm (Hildebrand & Kirby 2004).

Other possible sources of polarized dust emission at microwave frequencies are electric-dipole emission from 'spinnng-dust' grains, as well as magnetic-dipole emission from vibrating 'magnetic dust' grains (e.g. Draine & Lazarian 1998a,b, 1999; Lazarian & Draine 2000; Lazarian & Finkbeiner 2003; Ali-Haïmoud, Hirata & Dickinson 2009). Evidence for the existence of spinning dust exists in the strong correlations observed between the spatial distribution of thermal dust emission and that of anomalous emission at frequencies of 20–60 GHz. This anomalous emission cannot be accounted for by models using only the standard components of free–free, synchrotron and/or thermal dust emission. This dust-correlated anomalous emission is observed on both large scales (e.g. Kogut et al. 1996; Finkbeiner 2004; Finkbeiner, Langston & Minter 2004; Davies et al. 2006; Hildebrandt et al. 2007; Miville-Deschênes et al. 2008; Dickinson et al. 2009b) as well as in pointed observations of specific Galactic dust clouds (e.g. Finkbeiner 2004; Watson et al. 2005; Casassus et al. 2006; Dickinson et al. 2009a, 2010; Scaife et al. 2009; Planck Collaboration et al. 2011).

The polarization amplitude of spinning dust emission is likely to be small. Lazarian & Draine (2000), modelling the alignment of very small dust grains in the ISM, predict that spinning dust will be polarized by no more than ∼7 per cent at 2 GHz, falling to $\lesssim$0.5 per cent above frequencies of 30 GHz. Empirically, ultraviolet

observations of background-starlight polarization (caused by the same very small grains) indicate that these grains are not as well aligned with the local magnetic field as are larger grains (e.g. Martin 2007). Magnetic dust is expected to be polarized at much higher levels, as high as 40 per cent (Draine & Lazarian 1999). The only polarization observations of the anomalous emission to date have found low levels. Battistelli et al. (2006) report $3.4^{+1.5}_{-1.9}$ per cent towards the Perseus molecular cloud at 11 GHz, while Mason et al. (2009) report an upper limit of 3.5 per cent (99.7 per cent confidence level) towards the dark cloud Lynds 1622 at 9 GHz. López-Caraballo et al. (2011) used *WMAP* data to constrain the polarization towards the Perseus molecular cloud to be less than 1.0, 1.8 and 2.7 per cent at 23, 33 and 41 GHz, respectively. These observations are consistent with the polarization from spinning dust, but cannot rule out the existence of vibrating magnetic dust.

3.3 Free–free

Free–free (bremsstrahlung) emission is due to electron–electron scattering from warm ($T_e \approx 10^4$ K) ionized gas in the interstellar medium. In the optically-thin regime, and at radio frequencies, the brightness temperature is given by

$$T_b = 8.235 \times 10^{-2} a T_e^{-0.35} \nu_{GHz}^{-2.1} (1 + 0.08)(EM)_{cm^{-6}\,pc},$$

where T_e is the electron temperature, EM is the emission measure and a is a factor close to unity. The electron temperature in the warm ionized medium ranges from ≈3000 to ∼20 000 K but is ≈8000 K at the solar galacocentric distance. The spectrum follows a well-defined power law with a spectral index of −2.1 with only a small variation in temperature. At *WMAP* frequencies, the effective free–free spectral index is ≈−2.14 for $T_e \approx 8000$ K.

The well-determined spectrum can be used to separate free–free from other diffuse radio components, most notably, synchrotron (which is almost always steeper). However, due to the complexity of the components, and the limited frequency range of the *WMAP*, a cleaner separation can be achieved by using an appropriate spatial template. The free–free brightness temperature is proportional to $EM \equiv \int n_e^2\, dl$, that is, the integrated column density squared along the line of sight. Fortunately, this is also true of recombination lines such as the bright optical line, Hα. Maps of Hα therefore give an almost one-to-one tracer for radio free–free emission (Dickinson, Davies & Davis 2003) and they are now available for the full sky (Finkbeiner 2003). There is some dependancy on T_e and the local conditions, but these are relatively small. The main difficulty arises at low Galactic latitudes (typically $|b| < 5^\circ$) where dust absorption can reduce the Hα intensity by a large factor, thus rendering it useless for predicting radio free–free brightness. However, outside the Kp2 mask, almost all lines of sight have a small to negligible maximum correction factor; typical values are ≪1 mag. The correction factor can be estimated from the *IRAS* 100-μm redenning maps (Schlegel, Finkbeiner & Davis 1998). We therefore use the Finkbeiner (2003) composite Hα map as our standard free–free template, but also compare a similar map produced by Dickinson et al. (2003).

Free–free emission is intrinsically unpolarized because the scattering directions are random. However, a secondary polarization signature can occur at the edges of bright free–free features (i.e. H II regions) from Thomson scattering (Rybicki & Lightman 1979). This could cause significant polarization (∼10 per cent) in the Galactic plane, particularly when observing at high angular resolution. However, at high Galactic latitudes, and with a relatively low resolution, we expect the residual polarization to be <1 per cent.

4 THE CROSS-CORRELATION ANALYSIS

4.1 The method

The C-C method (described in Davies et al. 2006) assumes that the total intensity in every pixel is well modelled by a finite sum of separate emission mechanisms such that

$$\boldsymbol{I}_{tot}(\nu, \hat{\boldsymbol{n}}) = \sum_{i=1}^{n} T_i(\nu, \hat{\boldsymbol{n}}) \tag{2}$$

$$= \sum_{i=1}^{n} \theta_i(\nu, \hat{\boldsymbol{n}})\, T_i(\nu_{0i}, \hat{\boldsymbol{n}}), \tag{3}$$

where $\boldsymbol{I}_{tot}(\nu, \hat{\boldsymbol{n}})$ is the total emission at frequency ν in the direction (or map pixel) $\hat{\boldsymbol{n}}$, $T_i(\nu_{0i}, \hat{\boldsymbol{n}})$ is the emission from the ith template at the template frequency ν_{0i} [hereinafter simply $T_i(\hat{\boldsymbol{n}})$], and $\theta_i(\nu, \hat{\boldsymbol{n}})$ is the spectral shape of the emission template, normalized in every pixel such that $\theta_i(\nu_{0i}) = 1$. The C-C technique is applied to sky regions containing different pixels and assumes that the proportionality coefficients between the total intensity and each foreground component are constant within each region, that is, $\theta_i(\nu, \hat{\boldsymbol{n}})$ is independent of the position within each region, although they can vary from region to region:

$$\boldsymbol{I}_{tot}(\nu, \hat{\boldsymbol{n}}) = \sum_{i=1}^{n} \theta_i(\nu)\, T_i(\hat{\boldsymbol{n}}). \tag{4}$$

For the emission mechanisms studied in this work, we have $n = 3$ templates, although the C-C method can generally be extended to any number n. For any given *WMAP* frequency ν, an estimate of the parameters $\theta_i(\nu)$ can be computed by minimizing χ^2, as explained in Davies et al. (2006). In the component formalism of equation (4), we have

$$\theta_i(\nu) = \sum_{j=1}^{3} (A^{-1})_{ij} \left\{ \sum_{\hat{\boldsymbol{n}}}^{R} [T_j(\hat{\boldsymbol{n}})^{\mathrm{T}} \cdot \mathbf{M}_{SN}^{-1}(\nu, \hat{\boldsymbol{n}}) \cdot \boldsymbol{I}(\nu, \hat{\boldsymbol{n}})] \right\}, \tag{5}$$

where the sum over $\hat{\boldsymbol{n}}$ is the sum over all pixels in the sky region R, A_{ij} is the 3 × 3 template matrix $\sum_{\hat{\boldsymbol{n}}}^{R} \left[T_i(\hat{\boldsymbol{n}})^{\mathrm{T}} \cdot \mathbf{M}_{SN}^{-1}(\nu, \hat{\boldsymbol{n}}) \cdot T_j(\hat{\boldsymbol{n}})\right]$, and $\mathbf{M}_{SN}(\nu, \hat{\boldsymbol{n}})$ is the covariance matrix of the expected noise of the *WMAP* data and CMB signal (described in the next section). The objective is to invert the covariance matrix and compute the coefficients $\theta_i(\nu)$ for each of the three Galactic foreground components.

Within an area R of the sky, the C-C analysis relies on the morphological characteristics of a given component. The mean value of the template's emission within R (which can be thought of as a constant offset in the template's map) does not provide information for the purpose of recovering the signal relative to each individual component, as it has no morphological structure. Moreover, keeping these mean offsets in the templates fixed will bias the results of the C-C analysis. Since all templates, as well as all five *WMAP* maps, may have such uniform offsets, they can each be represented as a single uniform term in the sum of equation (3), that is, each template and data set have the form

$$T_i(\hat{\boldsymbol{n}}) = T_i'(\hat{\boldsymbol{n}}) - \delta_i', \tag{6}$$

where T' is an existing template map or *WMAP* data, and T_i is its true value in which all constant offsets have been removed. Equation (4) is then rewritten as

$$\boldsymbol{I}_{tot}'(\nu, \hat{\boldsymbol{n}}) = \sum_{i=1}^{n} \theta_i(\nu)\, T_i'(\hat{\boldsymbol{n}}) + \delta_{tot}(\nu), \tag{7}$$

where

$$\delta_{\rm tot}(\nu) = \delta'_{\rm tot}(\nu) - \sum_{i=1}^{n} \theta_i(\nu)\, \delta'_i. \quad (8)$$

If each analysis is limited to a single sky region covered by a single set of parameters $\theta_i(\nu)$, then each of the individual terms on the right-hand side of equation (8) is a monopole term. By extension, the total $\delta_{\rm tot}(\nu)$ must also be a constant monopole. Therefore, we can define a new template $T_{\rm off}(\nu, \hat{\boldsymbol{n}}) \equiv T_{\rm off} \equiv 1$ at all frequencies and all sky positions. Equation (7) can then be rewritten as

$$\boldsymbol{I}'_{\rm tot}(\nu, \hat{\boldsymbol{n}}) = \sum_{i=1}^{n+1} \theta_i(\nu)\, T'_i(\hat{\boldsymbol{n}}), \quad (9)$$

where $\theta_{(n+1)}(\nu) = \delta_{\rm tot}(\nu)$ and $T'_{(n+1)}(\hat{\boldsymbol{n}}) = T_{\rm off}$. The C-C analysis then proceeds just as in the case of a zero-offset but simply with an additional template term, and the value of $\delta_{\rm tot}(\nu)$ is returned along with the other n fit parameters, $\theta_i(\nu)$.

The introduction of an extra fitting parameter (the amplitude of the monopole term) increases the uncertainties returned in the other parameters of the C-C analysis. This effect is the largest at high Galactic latitudes where there is little variation in the foreground emission, that is, one should expect the correlation of the data with the monopole template to increase with increasing latitude even if a true constant offset does not exist in the data maps.

When these offsets are included in the C-C analysis, the reduced χ^2 is significantly better than without the offset. At the K band, it decreases by about 24 per cent for the temperature analysis and by about 8 per cent in the analysis of the polarized emission. These offsets are found to exhibit a distinct synchrotron-like frequency spectrum, whereas one would naively expect little correlation with frequency. This suggests that the Haslam et al. 408-MHz synchrotron template is dominating the fit offset terms.

4.2 Uncertainties

Writing the C-C error equation following the component formalism, the uncertainties on the fitted C-C coefficients for the ith template are

$$\delta\theta_i(\nu) = \sqrt{\sum_{\hat{\boldsymbol{n}}}^{R} \left\{ \left[T^{\rm T}(\hat{\boldsymbol{n}}) \cdot \mathbf{M}_{\rm SN}^{-1}(\nu, \hat{\boldsymbol{n}}) \cdot T(\hat{\boldsymbol{n}}) \right]^{-1} \right\}_{ii}}. \quad (10)$$

In equation (10), the covariance matrix $\mathbf{M}_{\rm SN} = \mathbf{M}_{\rm S} + \mathbf{M}_{\rm N}$, where $\mathbf{M}_{\rm N}$ and $\mathbf{M}_{\rm S}$ are the covariances of the instrumental noise and the CMB, respectively. The CMB signal covariance only has a significant contribution to the temperature analysis, where it dominates the instrumental noise.

We compute the signal covariance matrix in the usual way, taking the CMB power spectrum C_l from the *WMAP* best-fitting cold dark matter power-law spectrum model (Nolta et al. 2009). In practice, we take into account spatial correlations within 30° of a given pixel, effectively neglecting correlation values that are at most 0.5 per cent that of the pixel autocorrelation. The noise covariance in intensity is determined from the uncorrelated pixel noise as specified for each pixel in the *WMAP* data; this is an $N \times N$ diagonal matrix with the inverse of the observation number in each pixel on the diagonal ($\sigma_{\rm I} = \sigma_0/\sqrt{N_{\rm obs}}$).

We use the same strategy as in equation (10) to compute the errors in the polarization coefficients defined in Section 4.3 (equation 23). In the polarization analysis, the covariance matrix is dominated by the noise, which exceeds the contribution from the polarization power spectrum C_l^{EE} by two orders of magnitude.[4] $\mathbf{M}_{\rm N}$ is, to a good approximation, a diagonal matrix as the pixel-to-pixel noise correlation is at most 1 per cent of the diagonal term. We verified this by inspecting the $4 \times N \times N$ complete noise matrix available on the LAMBDA website, even though this is given at $N_{\rm side} = 16$ and our work is done using $N_{\rm side} = 32$ for the reasons introduced in Section 2. While it is true that we have no information on exact pixel-to-pixel correlations at $N_{\rm side} = 32$, the $N_{\rm side} = 16$ noise matrix suggests there are no large-scale noise correlations for the polarization analysis.

The polarization C-C analysis results are therefore computationally easier to determine than the temperature results, because we only need to compute N-dimensional arrays as opposed to the $N \times N$ needed in the temperature case. Therefore, we compute the noise for the total polarization in each pixel by combining noise in the Q and U maps at each frequency and properly taking into account Q–U correlations.

In every pixel $\hat{\boldsymbol{n}}$, we have a matrix

$$N(\hat{\boldsymbol{n}}) = \begin{pmatrix} QQ(\hat{\boldsymbol{n}}) & QU(\hat{\boldsymbol{n}}) \\ UQ(\hat{\boldsymbol{n}}) & UU(\hat{\boldsymbol{n}}) \end{pmatrix},$$

where $QQ(\hat{\boldsymbol{n}})$ and $UU(\hat{\boldsymbol{n}})$ are noises and $QU(\hat{\boldsymbol{n}})$ is the $\hat{\boldsymbol{n}}$-pixels Q–U noise correlation, all in terms of the observation number. Uncertainties on Q and U are given by the inverse of $N(\hat{\boldsymbol{n}})$:

$$\sigma_q(\hat{\boldsymbol{n}}) = \sigma_0 \sqrt{\{[N(\hat{\boldsymbol{n}})]^{-1}\}_{11}},$$

$$\sigma_u(\hat{\boldsymbol{n}}) = \sigma_0 \sqrt{\{[N(\hat{\boldsymbol{n}})]^{-1}\}_{22}}.$$

Propagating these noise terms to compute the uncertainty on $P = \sqrt{Q^2 + U^2}$, we obtain

$$\sigma_p(\hat{\boldsymbol{n}}) = \sqrt{\left[\frac{Q}{P}\sigma_q(\hat{\boldsymbol{n}})\right]^2 + \left[\frac{U}{P}\sigma_u(\hat{\boldsymbol{n}})\right]^2}. \quad (11)$$

$\sigma_p(\hat{\boldsymbol{n}})^2$ are the elements of the (diagonal) noise matrix $\mathbf{M}_{\rm N}$ for the total polarization P. The uncertainty on the polarized correlation coefficients is

$$\delta\rho_i(\nu) = \sqrt{\sum_{\hat{\boldsymbol{n}}}^{R} \left\{ \left[T^T(\hat{\boldsymbol{n}}) \cdot \mathbf{M}_{\rm N}^{-1}(\nu, \hat{\boldsymbol{n}}) \cdot T(\hat{\boldsymbol{n}}) \right]^{-1} \right\}_{ii}}. \quad (12)$$

When choosing the area over which to perform the C-C analysis, one should consider the trade-off between the uncertainties and the accuracy of the modelling. While it is more likely that in a small area a single fitting coefficient is sufficient to represent a given foreground, the uncertainties calculated with equations (10) and (12) decrease with the square root of the number of pixels considered. In the following, our choice to consider relatively large areas is a trade-off between these two competing aspects.

4.3 Polarization analysis and fractional polarization

When dealing with the C-C of the polarized emission, some preliminary comments are necessary. Since equation (4) holds for any measured intensity and polarization value, if templates from all Stokes parameters were available at some set of reference frequencies, that is, $Q_i(\nu_{0i}, \hat{\boldsymbol{n}})$ and $U_i(\nu_{0i}, \hat{\boldsymbol{n}})$, then equation (4) could be solved separately to determine the coefficients $\theta_i(\nu)$ in polarization

Equation (4), written for Q and U in each pixel $\hat{\boldsymbol{n}}$, becomes

$$Q_{\rm tot}(\nu, \hat{\boldsymbol{n}}) = \sum_{i=1}^{n} Q_i(\nu, \hat{\boldsymbol{n}}), \quad (13)$$

[4] On the diagonal elements, $\mathbf{M}_{\rm S} = 0.45\ \mu{\rm K}^2$, while $\mathbf{M}_{\rm N} = 55\ \mu{\rm K}^2$.

$$U_{\rm tot}(\nu, \hat{\boldsymbol{n}}) = \sum_{i=1}^{n} U_i(\nu, \hat{\boldsymbol{n}}). \quad (14)$$

Inserting the definitions of the Stokes parameters in terms of the fractional linear polarization f and the polarization angle γ, $Q = fI\cos(2\gamma)$ and $U = fI\sin(2\gamma)$, equations (13) and (14) become, respectively,

$$Q_{\rm tot}(\nu, \hat{\boldsymbol{n}}) = \sum_{i=1}^{n} q_i(\nu, \hat{\boldsymbol{n}})\, T_i(\nu, \hat{\boldsymbol{n}}), \quad (15)$$

$$U_{\rm tot}(\nu, \hat{\boldsymbol{n}}) = \sum_{i=1}^{n} u_i(\nu, \hat{\boldsymbol{n}})\, T_i(\nu, \hat{\boldsymbol{n}}), \quad (16)$$

where the correlation coefficients are

$$q_i(\nu, \hat{\boldsymbol{n}}) = f_i(\nu, \hat{\boldsymbol{n}})\theta_i(\nu)\cos[2\gamma_i(\nu, \hat{\boldsymbol{n}})], \quad (17)$$

$$u_i(\nu, \hat{\boldsymbol{n}}) = f_i(\nu, \hat{\boldsymbol{n}})\theta_i(\nu)\sin[2\gamma_i(\nu, \hat{\boldsymbol{n}})]. \quad (18)$$

To apply C-C as we did in the temperature analysis, we assume again that the coefficients $q_i(\nu, \hat{\boldsymbol{n}})$ and $u_i(\nu, \hat{\boldsymbol{n}})$ are constant over the analysed region of the sky.

We could still apply this procedure if we had complete information about the polarization angle for every foreground. For example, one could use simulated Galactic magnetic field maps to estimate the position angle of a thermal dust polarization template and the *K*-band polarization data as a synchrotron angle template as has been done by other authors (e.g. Page et al. 2007; Dunkley et al. 2009).

In this work, we wish to determine if useful knowledge can be extracted from the *WMAP* polarization data without making any assumptions about the dust or synchrotron polarization angles. It is possible to do so by considering the total polarization

$$P^2_{\rm tot}(\nu, \hat{\boldsymbol{n}}) \equiv f^2(\nu, \hat{\boldsymbol{n}})T^2(\nu, \hat{\boldsymbol{n}}) = Q^2(\nu, \hat{\boldsymbol{n}}) + U^2(\nu, \hat{\boldsymbol{n}}) \quad (19)$$

$$= \left[\sum_{i=1}^{n} q_i(\nu, \hat{\boldsymbol{n}})\, T_i(\hat{n})\right]^2 + \left[\sum_{i=1}^{n} u_i(\nu, \hat{\boldsymbol{n}})\, T_i(\hat{n})\right]^2. \quad (20)$$

Substituting q_i and u_i from equations (17) and (18), respectively, equation (20) can be rewritten as

$$P^2_{\rm tot}(\nu, \hat{\boldsymbol{n}}) = \sum_{i=1}^{n} f_i^2\theta_i^2 T_i(\hat{\boldsymbol{n}})^2 + \sum_{i=1}^{n}\sum_{\substack{j=1 \\ j\neq i}}^{n} \times f_i f_j \theta_i\theta_j T_i(\hat{\boldsymbol{n}})T_j(\hat{\boldsymbol{n}})\cos\left\{2\left[\gamma_i(\hat{\boldsymbol{n}}) - \gamma_j(\hat{\boldsymbol{n}})\right]\right\}. \quad (21)$$

[Note that we have dropped the frequency dependence in equation (21) for the sake of simplicity.] If we further assume that the polarization angles are equal for all emission components $[\gamma_i(\hat{\boldsymbol{n}}) = \gamma_j(\hat{\boldsymbol{n}})]$, then

$$P_{\rm tot}(\nu, \hat{\boldsymbol{n}}) = \sum_{i=1}^{n} \rho_i(\nu)\, T_i(\hat{\boldsymbol{n}}), \quad (22)$$

where

$$\rho_i(\nu) \equiv f_i(\nu)\,\theta_i(\nu). \quad (23)$$

Equation (22) is analogous to equation (4), but with the polarized-intensity correlation coefficients $\rho_i(\nu)$ rather than $\theta_i(\nu)$. Therefore, $\rho_i(\nu)$ can be computed by analogy with the C-C used to calculate the $\theta_i(\nu)$ given by equation (5). The fractional polarization coefficient $f_i(\nu)$ can be extracted for each component at each frequency from these two correlation coefficients:

$$f_i(\nu) = \frac{\rho_i(\nu)}{\theta_i(\nu)}, \quad (24)$$

with an uncertainty of

$$\delta f_i(\nu) = f_i(\nu) \times \sqrt{\left(\frac{\delta\rho_i}{\rho_i}\right)^2 + \left(\frac{\delta\theta_i}{\theta_i}\right)^2}. \quad (25)$$

The assumption of an equal polarization angle for all emission components is reasonable because the direction of all diffuse emission types is determined by the direction of the magnetic field. This assumption leads to a total polarization (summed over all emission components) with angles equal to the individual components, so that it is easily falsifiable by any measurement in which the total position angle changes with frequency. While such angle rotations with frequency are observed in the *WMAP* data, they are typically smaller than $\sim 20^\circ$ at a resolution of 4°. Moreover, the nearly-constant angle assumption is supported by Kogut et al. (2007) who found that the fits based on *K*-band (synchrotron-dominated) polarization angles or the starlight-polarization angles gave similar results, with a difference in the goodness-of-fit of about 1 per cent. The advantage of our approach is that no models are required to estimate the polarization angles.

The fractional polarization $f_i(\nu)$, as given in equation (24), is the ratio of *correlation coefficients*. One should keep in mind that negative values of the correlation coefficients $\rho_i(\nu)$, and therefore $f_i(\nu)$, are in fact physically meaningful. Anticorrelations between the polarization data and a total intensity template will occur in regions where the polarized emission drops with increasing total intensity. For example, this behaviour can be expected in regions where the polarization drops due to increased line-of-sight averaging towards regions of increasing column density. This point provides another reason to consider small areas of the sky where the polarization fraction is more likely to be constant.

4.4 Polarization noise bias

Given the Q and U values in each pixel, we calculate the polarized intensity using

$$P(\hat{\boldsymbol{n}}) = [\langle Q\rangle^2(\hat{\boldsymbol{n}}) + \langle U\rangle^2(\hat{\boldsymbol{n}})]^{1/2}, \quad (26)$$

and its associated uncertainty, where the direction $\hat{\boldsymbol{n}}$ denotes each $N_{\rm side} = 32$ ($\approx 2 \times 2\,{\rm deg}^2$) piece of the sky. The C-C analysis is then carried out on $P(\hat{\boldsymbol{n}})$ in each section of the sky defined in Section 5.

Polarization is a complex quantity which can be described by either its real and imaginary parts (Q and U), or its amplitude and phase (P and γ). If one assumes Gaussian statistics for Q and U, then the non-linear transformation into P and γ results in non-Gaussian statistics for these quantities. The key point for our analysis is that P has an asymmetric probability distribution (e.g. Simmons & Stewart 1985; Vaillancourt 2006) resulting in a positive bias. We have corrected for this bias using the formula

$$P_{\rm true} = 0 \qquad \text{for} \quad P/\sigma_p < \sqrt{2}, \quad (27)$$

$$P_{\rm true} \approx \sqrt{P^2 - \sigma_p^2} \quad \text{for} \quad P/\sigma_p > \sqrt{2}, \quad (28)$$

where σ_p is the polarization uncertainty defined in Section 4.2. While the last expression is not exactly precise, one can limit the effects of the bias by only using data above some polarization S/N level.[5] Such a bias can be estimated using Monte Carlo simulations as described in Section 5.1.

[5] No bias-correcting algorithm is exact. For more information, see Simmons & Stewart (1985), Vaillancourt (2006), and references therein.

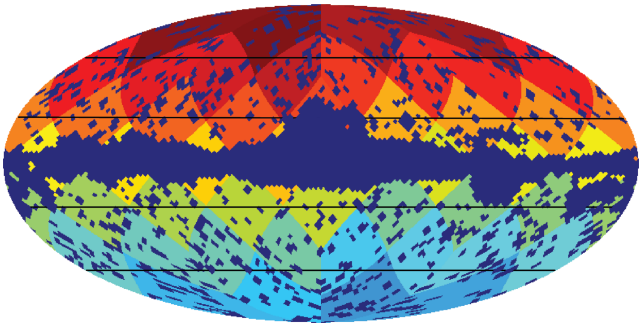

Figure 1. All-sky map with the 48 HEALPix $N_{\rm side} = 2$ regions in different colours with the KQ85 mask applied (dark blue). The horizontal black lines represent the isolatitude slices (latitude analysis) with $b = -90°/-50°$, $-50°/-20°$, $-20°/20°$, $20°/50°$, $50°/90°$.

5 RESULTS

We used C-C to compute, at each *WMAP* band, the emission coefficients of the three Galactic foreground components plus the offset monopole template. The analysis presented in this work was done in three different spatial configurations: on the whole sky outside the KQ85 Galactic mask (hereinafter the 'all-sky' analysis), in different isolatitude slices (hereinafter the 'latitude' analysis) with $b = -90°/-50°$, $-50°/-20°$, $-20°/20°$, $20°/50°$, $50°/90°$, and in 48 HEALPix $N_{\rm side} = 2$ regions (hereinafter the 'pixel' analysis). Selecting such partitions allows us to investigate how the foreground properties depend on direction and latitude (see also Kogut et al. 2007; Miville-Deschênes et al. 2008), while increasing the likelihood that the area we are analysing has a uniform fractional polarization (see Section 4.3). The best pixel area size among those tried is $N_{\rm side} = 2$; it is small enough that the assumption of constant polarization fraction is more likely to be satisfied, and large enough to contain spatial variations needed for the C-C method. Moreover, these areas match with previous works (e.g. Dunkley et al. 2009) allowing us to compare our results. Fig. 1 shows the sky locations of pixels used for the pixel analysis and the latitude slices used for the latitude analysis [see Table 3 (given later) for the mean latitudes and longitudes of each pixel].

From the C-C coefficients, we derive results on the relative level of each foreground in a given region, its frequency dependence on temperature and polarization, and its polarization fraction. We note here that it is not always possible to extract all this information at all frequencies and for all regions due to limited S/N. Therefore, we concentrate on results where there is 2σ statistical significance.

5.1 Tests on a simulated sky

In order to test the analysis method described in the preceding sections, we ran the CCA code on 500 noise realizations of a simulated sky with a given foreground parametrization. We created sky maps in both temperature and polarization, based on the three template temperature maps from Section 3, and scaled them using the average coefficients from Davies et al. (2006) at each frequency. We used a constant polarization fraction of 20 per cent for synchrotron, 3.5 per cent for dust,[6] and 0 per cent for free–free, and a polarization angle for both synchrotron and dust based on the *WMAP*5 *K*-band map. We also made a set of simulations with no dust polarization to compare cases without and without dust polarization. The CMB model is a Gaussian realization based on the *WMAP*5 concordance model. We used the LAMBDA $N_{\rm side} = 512$ I, Q and U inverse covariance matrices to produce an $N_{\rm side} = 512$ noise realization, which was added to the CMB and foreground maps, and then degraded to the resolution used in our analysis, that is, $N_{\rm side} = 32$.

We compared the results for each of the three components for the 500 realizations in each pixel. We focused on the results from the *K* band, where the data had the most significance. The recovered coefficients were, in general, close to the input values with no large biases. In temperature, the results were all within 3σ of the input value, except for one region for synchrotron (region 10 at 3.3σ) and one region for dust (region 12 at 3.1σ). The estimated uncertainties corresponded well to the scatter in the coefficients from the 500 realizations.

In polarization, the results for synchrotron and free–free were in good agreement with the input values. The mean recovered fractional polarization for synchrotron was 20.0 ± 0.3 per cent for the case with no dust polarization and 19.5 ± 0.3 per cent with dust polarization. For free–free, we obtained the mean values of -0.02 ± 0.18 and -0.04 ± 0.19 per cent for each case, respectively. This gives us confidence that the method works as expected and yields reasonable results.

However, the values recovered for dust did indicate bias, that is, an additional systematic error. The recovered fractional polarization was 0.003 ± 0.15 and 0.38 ± 0.15 per cent for the simulations with no dust polarization and 3.5 per cent dust polarization, respectively. This shows that simply averaging all the polarization values within a pixel will not yield a reliable estimate if the true value is as low as a few per cent. The situation improves when only using regions with significant ($>2\sigma$) detections. We found nine regions that were significant at the 2σ level, which resulted in a weighted average of 2.0 ± 0.2 per cent, that is, an underestimate by 1.5 per cent in absolute value. For the case with no dust polarization, no pixels were detected at greater than the 2σ level. Similarly, for free–free, we obtained an average value of 1.4 ± 0.4 per cent when using the six regions that were significant, that is, an overestimate of 1.4 per cent in absolute value.

From these tests, we conclude there is a bias in the average fraction polarization of $\approx$1.5 per cent, when the true fractional polarization is a few per cent or less. For a single region, we found cases where the bias is up to $\approx$5 per cent. The reason for this bias appears to lie in the cross-talk between the various components. For example, for regions we recover a significant dust polarization, with no dust polarization in the simulation, one can see a bias in either the synchrotron or the free–free polarization; this can explain why the average synchrotron polarization is slightly low, at the 1.7σ level, in the case where there is dust polarization. Nevertheless, we can still obtain useful constraints on the fractional polarization with the current data, keeping in mind the amplitude of possible biases.

Also, we can use the results of these simulations to estimate the significance of results for individual pixels. These will be discussed separately in the following sections on the synchrotron, free–free and dust results. For the cases where there is significant bias observed in the simulations, the fractional polarization results will be presented in terms of a statistical (stat) and systematic (sys) error. For example, for the significant dust regions above, the weighted average is 2.0 ± 0.2 (stat) $\pm$ 1.5 (sys) per cent.

[6] The 3.5 per cent polarization represents the polarization for the total dust-correlated component at the *K* band, which will be dominated by anomalous microwave emission, and virtually no contribution from thermal dust.

5.2 All-sky versus pixel analysis

We show in Fig. 2 the contribution of each foreground to the temperature emission as a function of frequency. These estimates, reported in Table 1, were obtained by multiplying the C-C coefficient for a given foreground at a given frequency with the root mean square (rms) of each foreground template outside the KQ85 mask. The figure clearly shows that the dust-correlated emission is the dominant component in temperature at all frequencies (see also Davies et al. 2006). The rise from 61 to 94 GHz indicates the high-frequency contribution of thermal dust, while at lower *WMAP* frequencies, there is a significant contribution from anomalous dust. It is this low-frequency dust-correlated emission that has been tentatively identified with emission from small rapidly spinning dust grains (Draine & Lazarian 1998a,b). However, the dust contribution to polarization is typically subdominant at low frequencies and will be discussed further in Section 5.4.

Given the C-C coefficients and foreground templates, and the assumption that the templates trace all the foreground emission, we can generate a model of the total foreground emission in the *WMAP* data. Comparing this model to the actual *WMAP* data yields a set of residuals which we use to estimate the extent to which a single fit coefficient (in the case of the all-sky analysis) represents the foregrounds across the whole sky. Results for the *K* band, where the foregrounds are the brightest, are reported in Fig. 3 (left-hand panels) for both temperature and polarization. In the all-sky temperature residuals, the largest residuals occur near the Galactic plane, particularly near the Galactic Centre. This feature has been interpreted as the Galactic haze, possibly associated with annihilating particles (Finkbeiner et al. 2004; Cumberbatch et al. 2009). However, this feature is not evident in the pixel analysis where we compute separate C-C coefficients in 48 different regions (Fig. 3, right-hand panels). This is a consequence of a varying synchrotron spectral index, which is somewhat flatter than the average near the Galactic Centre, due to a diversified population of electrons in the Galaxy.

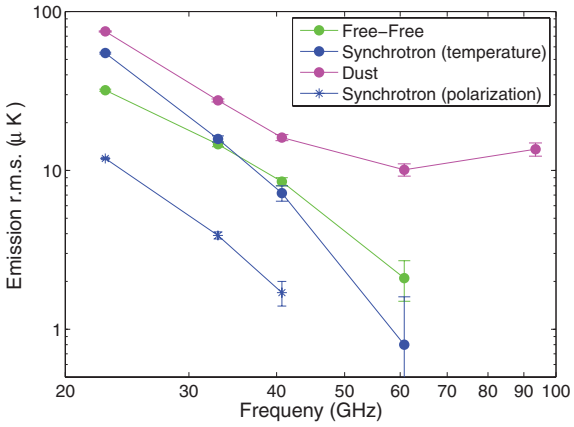

Figure 2. rms emission spectrum of Galactic foreground components from the all-sky (KQ85 cut) intensity and polarization analyses, in μK. Only the polarized synchrotron emission is plotted as the dust-correlated and free–free-correlated polarized emissions are consistent with zero for the all-sky region.

Table 1. Emission rms values for the all-sky analysis in both temperature and polarization for synchrotron (S), dust (D) and free–free (F–F) in the five *WMAP* bands. These values are plotted in Fig. 2.

	K band	*Ka* band	*Q* band	*V* band	*W* band
			Temperature rms emission (μK)		
S	54.8 ± 0.7	15.8 ± 0.7	7.2 ± 0.8	0.8 ± 1	-0.8 ± 1.3
D	75.0 ± 0.6	27.6 ± 0.6	16.1 ± 0.7	10.1 ± 0.9	13.6 ± 1.3
F–F	32.0 ± 0.5	14.6 ± 0.5	8.5 ± 0.5	2.0 ± 0.6	-0.2 ± 1.1
			Polarization rms emission (μK)		
S	11.9 ± 0.2	3.9 ± 0.2	1.7 ± 0.3	0.1 ± 0.4	0.1 ± 0.4
D	-0.2 ± 0.1	-0.1 ± 0.2	0.0 ± 0.3	0.1 ± 0.3	0.0 ± 0.4
F–F	-0.2 ± 0.1	-0.3 ± 0.2	-0.2 ± 0.2	0.0 ± 0.4	0.0 ± 0.6

Bright residuals in the all-sky analysis are also concentrated on the well-known Galactic spurs such as the North Polar Spur (NPS) above and below the Galactic Centre region. These spurs are known to have a slightly steeper synchrotron spectral index than the average and therefore are not well suited for the all-sky polarization analysis. Furthermore, these large coherent features are expected to have significantly different fractional polarizations. The residual map for the 48-pixels analysis (Fig. 3) shows less extended structure, with more localized residuals near the mask edge. This indicates that a local analysis is more suited to handle the complex foreground variations. In summary, Fig. 3 shows that it is suboptimal to model foregrounds without considering that they are spatially varying in the sky.

To have a quantitative understanding of the goodness-of-fit, we compute the reduced χ^2 for each type of analyses, both in temperature and polarization. These are reported for the *WMAP K* and *Ka* bands in Table 2. Again we see that neither the all-sky nor the latitude analysis is as accurate as the pixel analysis, especially in the *K*-band polarization. A limitation of the pixel analysis is that, in any given pixel, there may not be sufficient data points to yield S/N > 1. This is a particular problem for high frequencies (mostly the *V* and *W* bands) in polarization. In most cases, we will be limited to studying the *WMAP* foregrounds at the *K* band only. The 48 emission coefficients in the *K* band, for each foreground component in intensity and polarization, are reported in Table 3.

5.3 Synchrotron

Synchrotron is the dominant contribution to the polarized *K*- and *Ka*-band emission, especially in the Northern hemisphere, as reported in Table 3, because of the strong emission associated with the NPS. On the other hand, synchrotron is comparable to anomalous dust emission in temperature, and again its emission is more intense in the northen part of the sky.

From the all-sky analysis, using the *K* and *Ka* bands and the corrected Haslam et al. map described before, we find $\beta_s = -3.32 \pm 0.12$ in intensity and -3.01 ± 0.03 in polarization, where the errors come from the uncertainties on the C-C coefficients. The smaller polarization uncertainties occur here because synchrotron is the dominant polarized foreground at low frequencies, as opposed to the intensity analysis where the dust-correlated and free–free-correlated emissions are comparable to the synchrotron. These synchrotron spectral indices are in good agreement with previous results, that is, $\beta_s \approx -3$ (e.g. Miville-Deschênes et al. 2008).

From the pixel analysis, we find that the synchrotron emission is polarized from ≈5 per cent in some regions at low Galactic latitudes up to ≈40 per cent at high latitudes, as reported in Fig. 4 (top panel). In Fig. 5, the same quantity is plotted as a function of the mean Galactic latitude of each region. The decline of the polarized emission at low latitudes is well known in the literature (e.g. Wolleben et al. 2006) and is interpreted as a depolarization

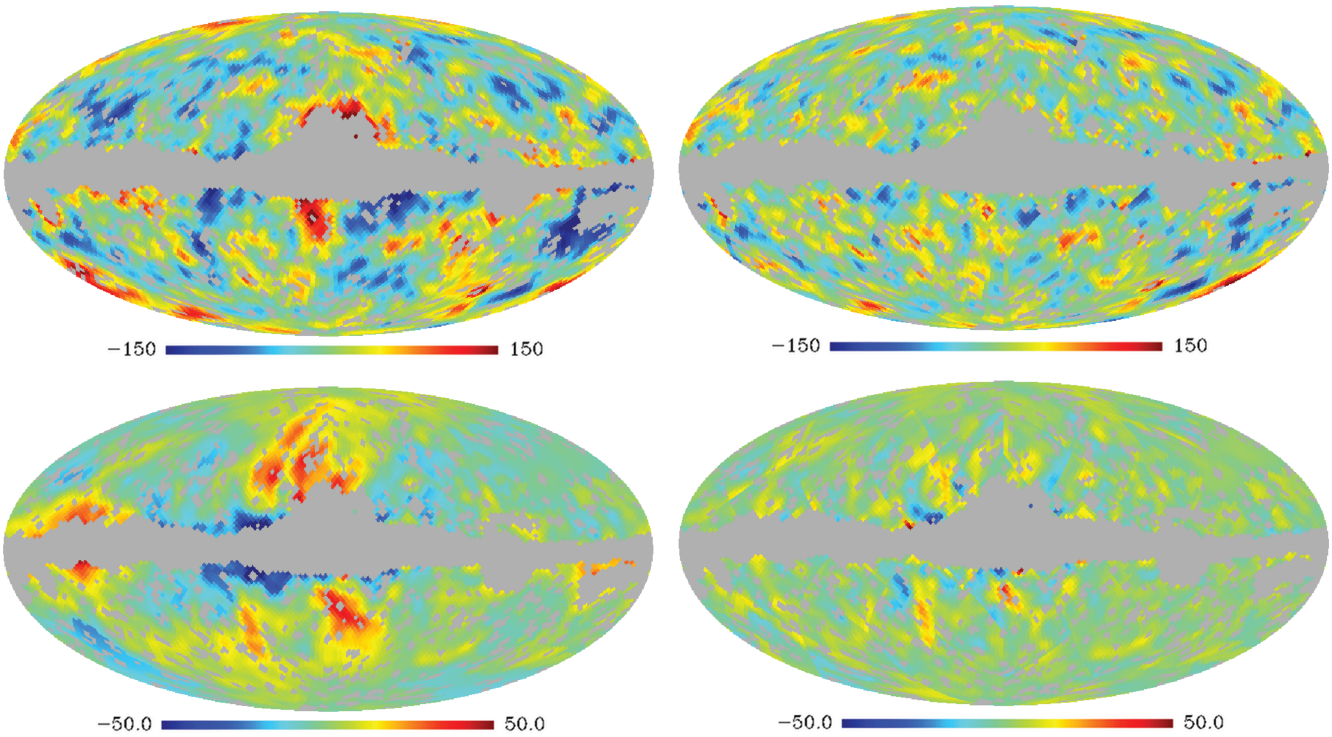

Figure 3. Residual maps (on Mollweide projection) for the *WMAP K*-band temperature (top panels) and polarized intensity (bottom panels) analyses. The results using the all-sky (KQ85 cut) region are reported (left-hand panels) together with the results using the 48 HEALPIX $N_{side} = 2$ regions (right-hand panels). The colour-scale is in units of μK.

Table 2. Reduced χ^2 for the three analysis types implemented in this paper. The values are the average over the different regions (when more than one is used).

	K band	*Ka* band
All-sky temperature	0.94	0.68
All-sky polarization	5.37	0.73
Latitude temperature	0.97	0.74
Latitude polarization	3.72	0.56
Pixel temperature	0.65	0.48
Pixel polarization	1.65	0.30

effect near the Galactic plane ($|b| \lesssim 20^\circ$) due to integration along the line of sight of emission with different polarization angles. The average polarization fraction in the pixel regions with ($|b| < 20^\circ$) is 8.6 ± 1.7 (stat) $\pm$ 0.5 (sys) per cent. Uncertainties at high latitudes are usually larger than at low latitudes because the templates have less variations in their structure at high latitudes. This renders the C-C analysis increasingly degenerate, as explained in Section 4.2. Nevertheless, the synchrotron fractional polarization at high Galactic latitudes is in the range ∼10–40 per cent with the average value of 19.3 ± 0.8 (stat) $\pm$ 0.5 (sys) per cent and standard deviation of ±11.0 per cent ($|b| > 20^\circ$). As discussed in Section 5.1, the synchrotron values are the most robust of the three components, and we believe the errors from the C-C method are representative, even after averaging.

Our estimate of the synchrotron fractional polarization is consistent with other work at the 1σ level. Kogut et al. (2007) computed the fractional synchrotron polarization by dividing the polarized emission (estimated using a pixel-by-pixel frequency fit), by a synchrotron intensity map (based on a maximum-entropy method analysis; Hinshaw et al. 2007). They find a typical fractional synchrotron polarization of 5–25 per cent. However, since this intensity map was computed ignoring a possible contribution from anomalous dust, the synchrotron intensity may be overestimated, resulting in an underestimate of the fractional polarization. On the other hand, Miville-Deschênes et al. (2008) included a spinning dust contribution to the total *K*-band intensity, and obtained a higher synchrotron fractional polarization, up to 40 per cent. The fact that our results are compatible with these implies that in most of the pixel regions the assumptions described in Section 4.3 are reasonable.

We have computed the synchrotron spectral index in every pixel with S/N > 2 again using only the *K* and *Ka* bands (see Table 4). The problem in this case is that the pixels with S/N > 2 are few, and we conclude that the C-C technique is not appropriate for a detailed spectral index analysis. None the less, the spectral indices in polarization are consistent with other analyses (e.g. Dunkley et al. 2009 who find $\beta_s \simeq -3$); we find an average value is $\beta_s = -3.24 \pm 0.20$.

In temperature, the results are not compatible with polarization, with an average spectral index of $\beta_s = -2.02 \pm 0.20$. This is clearly too flat and must be an artefact of the analysis. We checked that these results, especially in the five low-β_s regions, are not due to a high correlation between synchrotron and dust. Without sufficient differences in spatial morphology between synchrotron and dust, confusion can occur between the two components in the C-C analysis. As we expected, the dust and synchrotron templates are correlated with an all-sky (outside the KQ85 mask) correlation coefficient of $r = 0.48$. In the regions where high synchrotron spectral indices are observed (4, 5, 16, 27 and 32), the correlation between dust and synchrotron is higher ($r = 0.71$). This suggests

Table 3. Results of the pixel analysis. Here we report the pixel region number, the number of data points, the average latitude and the average longitude of each region, the synchrotron-correlated temperature emission at the K band in μK, the dust-correlated temperature emission at the K band and at the W band in μK, and the fractional polarization percentage of synchrotron, anomalous dust and free–free at the K band. Bold faces are used to emphasize a component with a temperature emission higher than 60 μK at the K band and 15 μK at the W band, and are use to indicate regions where a particular component is found to be more than 2σ significantly polarized. We indicate 2σ upper limits when in that region the fractional polarization is compatible with zero. No data for fractional polarizations indicate upper limits reaching 100 per cent. In column 5, 6 and 7, we display detections that are significant at the 1σ level. Note that the systematic uncertainties are not included here and can be significant when the polarization fractions are low, that is, less than a few per cent (see Section 5.1). The χ^2 values from the temperature and polarization analyses at the K band are also reported.

Pixel	Pixels	⟨Latitude⟩	⟨Longitude⟩	Synchrotron K	Dust K	Dust W	Synchrotron per cent	Dust per cent	Free–free per cent	$\chi^2_{\rm T}$	$\chi^2_{\rm P}$
1	207	65.7	46.2	38.9 ± 3.8	19.6 ± 4.2	11 ± 5.3	$\mathbf{40.6 \pm 4.7}$	<11.0	–	0.45	0.41
2	214	66.7	134.8	–	–	–	–	–	–	0.31	0.81
3	214	66.8	224.5	–	9.5 ± 3.2	–	–	–	–	0.49	0.73
4	202	67	318	30.6 ± 3.4	9.5 ± 3.4	–	$\mathbf{23.8 \pm 3.6}$	–	<11.6	0.84	0.41
5	189	42.3	21.3	49.5 ± 3.3	56.8 ± 4.3	–	$\mathbf{26.1 \pm 2.4}$	$\mathbf{7.2 \pm 2.3}$	–	0.45	3.01
6	195	43	69.7	–	19.9 ± 3.2	6.2 ± 3.5	–	$\mathbf{10.6 \pm 4.9}$	–	0.49	2.11
7	209	42	110.3	9.9 ± 2.6	32.7 ± 3.4	7.4 ± 3.7	$\mathbf{17.8 \pm 7.5}$	<5.0	–	0.55	0.75
8	195	41.9	159.8	10.2 ± 4.5	30.8 ± 4.3	8.4 ± 4.8	42.4 ± 21.6	<7.6	–	0.49	1.42
9	211	41.7	200.1	8.7 ± 3.7	–	–	16.7 ± 14.4	–	–	0.56	0.22
10	232	41.6	250.8	12.9 ± 3.4	12.8 ± 2.8	–	$\mathbf{18.3 \pm 7.6}$	<12.8	<12.4	0.60	0.31
11	205	42.1	289.8	16.8 ± 2.9	23.8 ± 3.4	–	$\mathbf{21.3 \pm 6.2}$	–	<11.6	0.47	1.05
12	214	42.4	339.6	25.7 ± 4.1	43.5 ± 4.2	–	$\mathbf{22.5 \pm 5.6}$	<5.8	–	0.37	2.16
13	44	30.9	4.1	21.1 ± 4.5	$\mathbf{69.6 \pm 4.9}$	14.1 ± 5.2	$\mathbf{44.3 \pm 12.8}$	<3.6	<6.4	1.32	2.32
14	200	21.1	44.9	$\mathbf{104.8 \pm 4.4}$	54.7 ± 4.3	–	$\mathbf{23.7 \pm 1.4}$	–	–	0.98	2.02
15	158	21.4	88.6	–	$\mathbf{110.5 \pm 3.4}$	17.2 ± 3.4	–	<1.6	<5.0	0.63	1.87
16	167	22.7	135	$\mathbf{81.9 \pm 5.3}$	$\mathbf{76.4 \pm 4.2}$	–	$\mathbf{19.8 \pm 1.9}$	–	7.6 ± 4.8	0.61	0.28
17	211	20.1	180.5	22.9 ± 3.9	$\mathbf{80 \pm 3.4}$	20.9 ± 4.0	$\mathbf{29.6 \pm 6.9}$	2.6 ± 1.3	–	2.25	1.39
18	209	20.3	225.1	–	$\mathbf{62.1 \pm 4.3}$	$\mathbf{26.8 \pm 4.4}$	–	<2.4	–	1.10	0.43
19	172	22.6	270.4	12.2 ± 4.4	22.9 ± 3.7	–	$\mathbf{34.9 \pm 16.2}$	<9.8	<3.8	1.26	1.22
20	162	22.9	315	$\mathbf{97.3 \pm 3.5}$	45.2 ± 4.6	–	$\mathbf{14.8 \pm 1.1}$	<7.2	–	0.52	2.10
21	28	−8.1	23.5	$\mathbf{59.7 \pm 5.9}$	54.3 ± 7.2	–	–	8.4 ± 5.9	–	0.81	6.08
22	86	0	66.1	48.3 ± 6.7	$\mathbf{61.2 \pm 5.2}$	–	5.7 ± 3.4	<5.0	<6.0	0.50	5.14
23	50	−5.9	110.4	33.1 ± 5.4	$\mathbf{84.1 \pm 6.4}$	–	$\mathbf{10.8 \pm 5.1}$	$\mathbf{6.0 \pm 1.8}$	<7.0	0.78	1.33
24	53	6.3	158.1	12.8 ± 6.2	$\mathbf{102.5 \pm 6.1}$	29.4 ± 7.2	43.9 ± 26.9	2.3 ± 2	–	0.57	1.30
25	88	5.6	203.6	–	$\mathbf{100.9 \pm 5.3}$	$\mathbf{22.7 \pm 6.0}$	–	2.8 ± 1.8	8.7 ± 5.1	1.78	0.84
26	64	3	244.4	11.7 ± 7.6	54.3 ± 5.5	–	–	<5.8	<3.2	1.15	0.46
27	74	−0.8	291.3	$\mathbf{58.2 \pm 4.7}$	$\mathbf{60.1 \pm 4.3}$	–	$\mathbf{9.1 \pm 2.2}$	2.7 ± 1.7	<12.6	0.90	1.11
28	16	−12.2	336.7	$\mathbf{88 \pm 17.2}$	35.8 ± 16.2	–	–	–	–	0.88	2.80
29	180	−22.3	1.5	$\mathbf{62.5 \pm 4.9}$	$\mathbf{64.9 \pm 3.5}$	13.8 ± 4.1	$\mathbf{19.6 \pm 2.6}$	–	–	0.47	0.49
30	214	−21	45.2	39.7 ± 5.6	$\mathbf{74.4 \pm 5.6}$	15.8 ± 5.6	6.8 ± 3.6	<4.0	–	1.00	2.20
31	177	−21.8	89.4	–	$\mathbf{88.1 \pm 3.6}$	$\mathbf{28.3 \pm 4.4}$	–	<2.0	–	0.49	0.81
32	195	−19.9	135.2	34.2 ± 4.7	$\mathbf{80 \pm 4.1}$	12.6 ± 4.6	$\mathbf{36.9 \pm 6}$	1.5 ± 1.4	<6.2	0.99	1.17
33	102	−24.9	178	17.8 ± 3.5	$\mathbf{107.1 \pm 3.8}$	$\mathbf{30.2 \pm 4.0}$	$\mathbf{52.9 \pm 12.5}$	<2.4	<6.0	1.13	0.82
34	150	−20.5	226.9	$\mathbf{72.6 \pm 6.4}$	$\mathbf{104.8 \pm 5.2}$	$\mathbf{22.7 \pm 7.4}$	$\mathbf{7.1 \pm 2.3}$	$\mathbf{3.2 \pm 1.5}$	<10.2	0.45	0.85
35	145	−22.2	272.1	–	51.1 ± 5.2	–	–	$\mathbf{4 \pm 1.8}$	<2.2	0.50	0.74
36	181	−21	314	39 ± 4.6	$\mathbf{79.3 \pm 3.5}$	14.3 ± 4.4	$\mathbf{26.4 \pm 4.2}$	<2.2	–	0.49	1.23
37	207	−41.8	19.3	24.7 ± 4.5	18.7 ± 6	–	$\mathbf{21.6 \pm 6.6}$	–	–	0.39	0.61
38	191	−42.7	69.6	–	25.3 ± 3	–	–	<6.6	–	1.05	2.12
39	206	−41.9	109.9	10.8 ± 3.7	16.4 ± 2.4	–	–	<10	–	0.47	0.60
40	202	−42	159.8	–	$\mathbf{90.5 \pm 3.2}$	–	–	<2.6	–	0.98	1.09
41	213	−42.8	200	–	47.8 ± 2.6	7.2 ± 2.8	–	<3.8	<8.4	1.27	0.80
42	201	−42.2	251.1	–	13.8 ± 4.4	–	–	–	–	0.59	0.96
43	217	−42.4	290.5	–	$\mathbf{66 \pm 4}$	$\mathbf{15.7 \pm 4.4}$	–	<2.2	<10.6	0.33	0.70
44	215	−41.6	339.7	33.8 ± 4.2	13.1 ± 4.3	–	$\mathbf{38.5 \pm 5.6}$	–	–	0.56	1.30
45	203	−66.4	45.7	11.8 ± 2.8	11.5 ± 3.2	–	$\mathbf{25.2 \pm 9.1}$	$\mathbf{31.7 \pm 11.7}$	–	0.40	0.32
46	202	−66.3	134.4	20.5 ± 2.9	–	–	–	–	–	0.55	1.60
47	206	−66.7	224.2	10.3 ± 3.6	12.7 ± 2.5	–	13.8 ± 8.8	<9.8	–	0.91	0.72
48	193	−65.7	313.6	–	–	–	–	–	–	0.37	0.63

again that, in temperature, the C-C method in some pixel regions is not able to correctly separate the synchrotron, free–free and dust components. In fact, most of the areas where the spectral index is biased by this effect are the ones that have problems for synchrotron in our simulations, for example, regions 16, 27 and 32. Moreover, when fitting over larger regions, the spectral index moves to more typical values of $\beta_{\rm s} \approx -3$. The same difficulty with the C-C analysis was found in previous work, for example, Davies et al. (2006), where

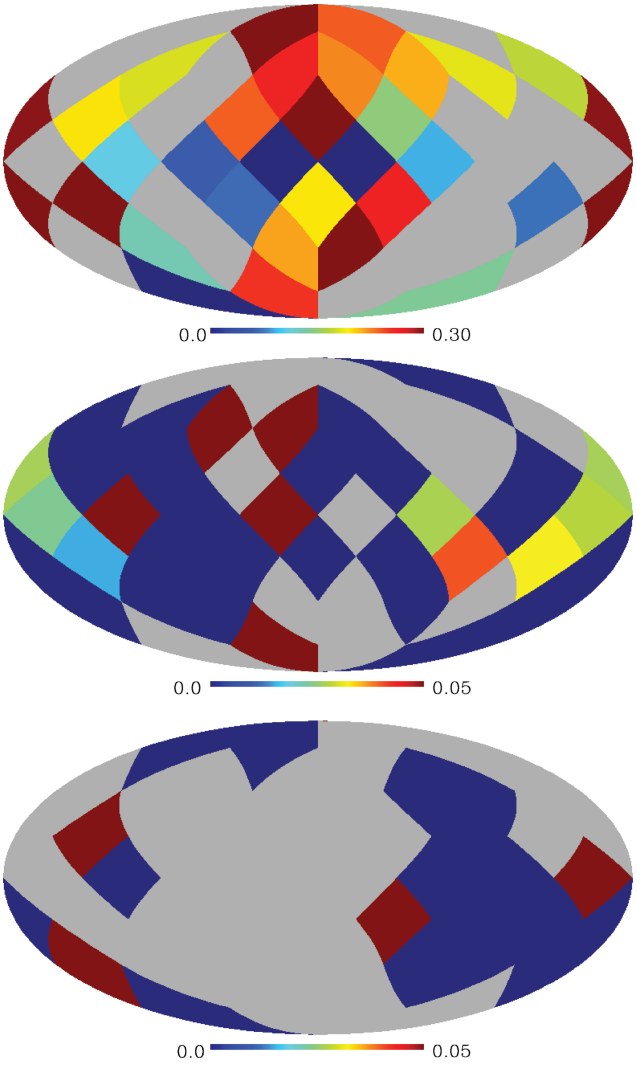

Figure 4. Synchrotron-correlated (top panel), dust-correlated (middle panel) and free–free-correlated (bottom panel) fractional polarizations in the 48 regions of the *K*-band pixel analysis. The regions compatible with a zero polarization fraction within 1σ are plotted in blue. Regions with $2\sigma_p >$ 30 per cent, or with negative fractional polarization, are plotted in grey.

the introduction of the 0.4-GHz point of Haslam et al. was needed to obtain meaningful spectral index values. However, we note that this problem is most significant at the higher frequency channels above 33 GHz, while at the *K* band, the coefficients are not strongly affected. Indeed, the spectral index computed from the weighted mean *K*-band coefficient alone, which corresponds to the mean spectral index between 408 MHz and 23 GHz, is $\beta_s = -2.97 \pm 0.01$.

5.4 Dust

It is clear from the all-sky analysis of Fig. 2 that the total unpolarized signal across all five *WMAP* bands is dominated by dust-correlated emission. The rise in dust emission from 61 to 94 GHz is consistent with the expectation of thermally emitting dust. The drop with frequency from 22 to 61 GHz has been termed 'anomalous' dust-correlated emission and has been attributed to such sources as spinning dust emission (e.g. Draine & Lazarian 1998a,b) and dust-correlated synchrotron emission (Bennett et al. 2003). The results

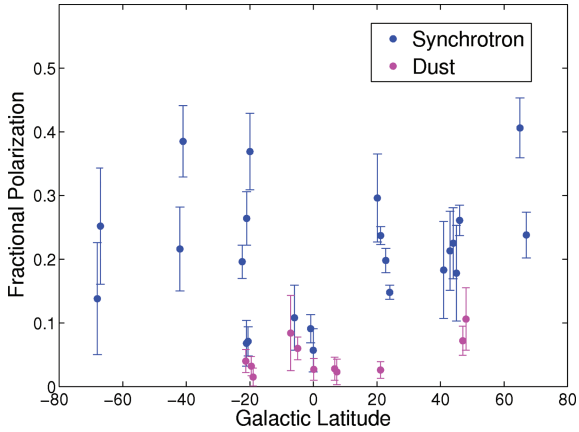

Figure 5. Synchrotron- and dust-correlated fractional polarization of the *WMAP K* band as a function of mean Galactic latitude in the 48 regions of the pixel analysis. We plot only regions where $f_p > \sigma_{f_p}$.

in Fig. 2, and the *K*–*Ka* spectral index for anomalous dust of $\beta_d \approx -2.5$, are consistent with the results of Davies et al. (2006).

The results for emission presented in Table 3 show that dust emission also dominates the unpolarized *K*-band emission for most of the sky in the pixel analysis. We find that the dust-correlated emission is dominant at low frequencies in many pixels even where the thermal dust emission is not present (e.g. pixels 16, 22, 23, 27 and 40).

Fig. 4 shows the polarization fraction of each foreground at the *K* band, computed using equation (24). The same values are reported in Table 3. As expected, synchrotron emission is highly polarized, while dust and free–free emission almost unpolarized. We compared the values found in various pixels with the distributions obtained from simulations. As a general comment on the simulations, we can say that (i) the range of the recovered dust polarization fraction, assuming the null hypothesis, is typically 5–10 per cent and varies between a few per cent and 25 per cent (for regions very distant from the Galactic plane, e.g. 2, 3, 47, 48); (ii) the distributions from simulations with and without dust polarization are, in general, very similar, although higher mean polarization values are not always associated with the case corresponding to the polarized dust (this may indicate cross-talk with other components); and (ii) the variance

Table 4. Synchrotron spectral index values in different pixel regions from the intensity and polarization analyses at the *K* and *Ka* bands. Only the regions with a significant result are reported ($\sigma_{\beta_s} < 1.0$).

Pixel	β_s temperature	β_s polarization
1	-2.88 ± 0.92	-3.01 ± 0.56
4	-1.79 ± 0.65	-3.58 ± 0.98
5	-1.85 ± 0.41	-3.39 ± 0.64
14	-2.02 ± 0.30	-3.44 ± 0.41
15	–	-3.22 ± 0.95
16	-1.35 ± 0.34	-3.50 ± 0.89
20	-2.28 ± 0.25	-4.13 ± 0.94
21	-2.30 ± 0.73	–
22	–	–
27	-1.48 ± 0.45	–
28	–	–
29	–	-2.81 ± 0.99
32	-1.73 ± 0.92	-2.53 ± 0.71
44	–	-3.36 ± 0.82

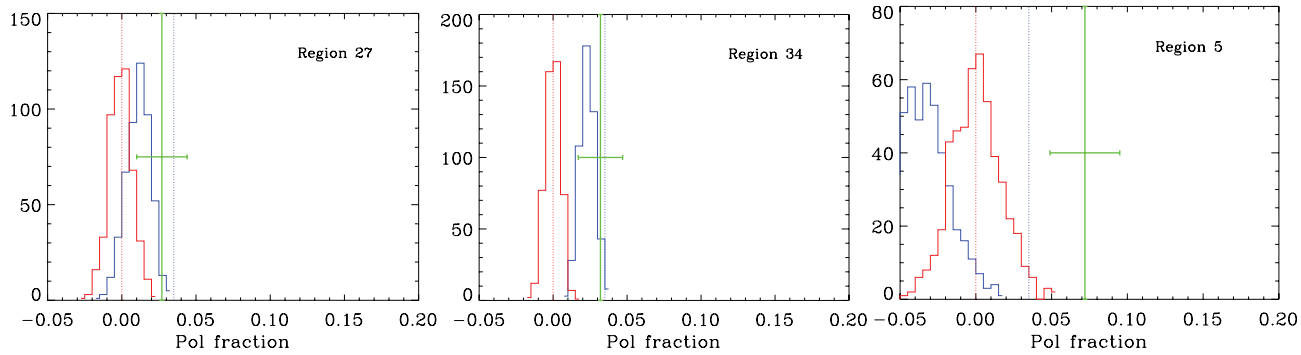

Figure 6. Histograms of the K-band dust polarization fraction for three regions, from 500 realizations, for the case with no dust polarization (red line) and with 3.5 per cent dust polarization (blue line). The input values are shown as the vertical dotted lines. The green line and error bar represent the best-fitting value and its 1σ uncertainty from the real data, respectively.

in the distributions is typically similar to the error bars computed by the CCA on real data.

When we compare the detected values of the polarization fraction in the K band with the distribution, we find that in some pixels they exceed the tail of the simulation distribution. The pixels for which the simulation-recovered values are always below the (real) detected dust polarization are 5, 17, 21, 23, 25, 27, 34 and 35 (see examples in Fig. 6).[7] In some regions (5, 6, 17, 21, 23, 24, 25, 27, 32, 34, 35 and 45), the detections are at more than the 2σ level. Some of these regions also show a (small) increase in synchrotron polarization with respect to simulation results (e.g. 5, 17 and 32), with an accompanying anticorrelation with the dust values. Indeed, in some cases, the recovered dust polarization fraction becomes slightly negative, such as in region 5 (see Fig. 6), which is evidence of cross-talk between components. Six regions (5, 17, 23, 34, 35 and 45) out of the 48 exceed the simulated distributions at the 99th percentile and are individually significant at $>2\sigma$. They showed fractional polarizations in the range 2.6–7.2 per cent except for the anomalous pixel 45, which appears to have a high polarization fraction of 32 ± 12 per cent, detected at a significance level of 2.7σ. This region does not contain any strong foreground features in total intensity or in polarization. Additionally, the simulation recovers the correct polarization but with a relatively large uncertainty. The detected value in the real data is well outside the distribution, as shown in Fig. 7. This region should be investigated further with higher sensitivity data (e.g. 9-year *WMAP*, *Planck*).

Although we cannot rely heavily on individual pixels, we can still continue, knowing that there can be biases of up to $\approx$5 per cent in any given region, and $\approx$1.5 per cent when averaging significant ($>2\sigma$) pixels, as discussed in Section 5.1. Furthermore, we can choose pixels that in the simulations were able to recover the correct dust amplitude within 1σ of the true value (regions 6, 12, 25, 33, 34, 35, 39 and 45). Although these may not be completely representative of the real data, they should be more reliable than simply averaging all or just significant pixels. For these, we find a weighted average of 3.2 ± 0.9 (stat) $\pm$ 1.5 (sys) per cent. We do not claim this as a real detection, since this is only a $\approx 2\sigma$ detection when considering the overall bias seen in the simulations described in Section 5.1. However, it is clear that the average K-band dust polarization fraction is less than about 5 per cent at 95 per cent confidence.

[7] For comparison, the number of pixels in which the fractional polarization is always below the distribution is two.

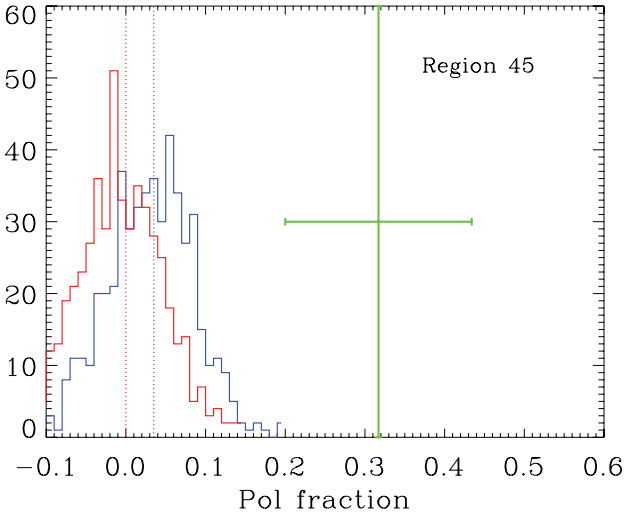

Figure 7. Histogram of the K-band dust polarization fraction for region 45, from 500 realizations, for the case with no dust polarization (red line) and with 3.5 per cent dust polarization (blue line). The input values are shown as the vertical dotted lines. The green line and error bar represent the best-fitting value and its 1σ uncertainty from the real data, respectively.

A comparison of the dust and synchrotron values at the K band (Fig. 5; as a function of Galactic latitude) shows that the K-band synchrotron polarization increases from $f_s \sim 5$ per cent to $\sim$40 per cent, while the dust remains fairly constant within the error bars at $f_d \sim$ 2–10 per cent in the pixels where significant dust polarization emission is found. Over most of the sky dust is found to be unpolarized, with a 2σ upper limit on fractional polarization of about 5 per cent in 17 pixel regions and about 10 per cent in four other regions.

Given the limitations of our results, particularly at frequencies above 33 GHz, we cannot make a detailed analysis of the frequency dependence of the dust polarization. Fig. 8 reports the rms of the dust polarization emission. The fractional polarization for these same data are plotted in Fig. 9 (pixel 21 has been removed from this plot as the temperature analysis yields negative C-C coefficients). Here we report just the K-, Ka-, and Q-band results, as the higher frequency data have S/N less than 1σ. While the fractional polarization data do exhibit a slight frequency dependence, the uncertainties are quite large. Due to these large uncertainties, we provide only a broad discussion, rather than a detailed analysis, of these results in the remainder of this section.

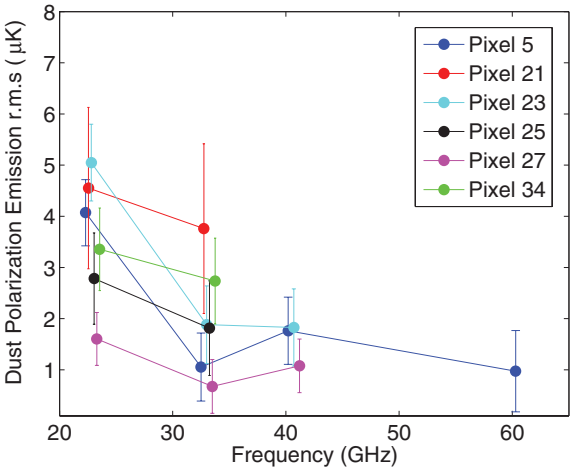

Figure 8. Dust-correlated polarized emission rms in μK as a function of frequency in the pixel analysis. We report only the six pixel regions where there is 2σ significant emission in the *K* band.

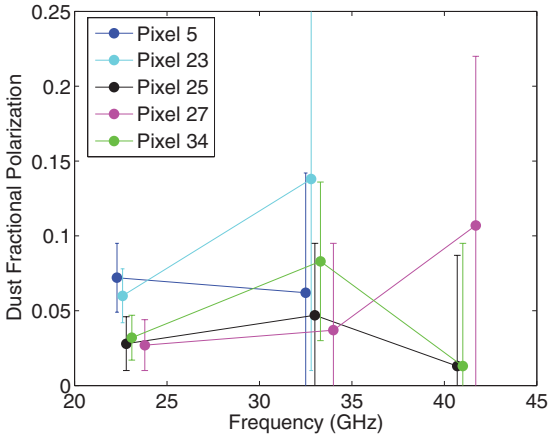

Figure 9. Dust-correlated polarization fraction as a function of frequency in the pixel analysis. We report only the five pixel regions where there is a $>1\sigma$ result in the *K* band that also have a non-zero value at the *Ka* and *Q* bands.

In the all-sky analysis (Fig. 2), the total emission from the anomalous dust component appears to dominate the thermal dust component for frequencies below 61 GHz (*V* band). We find similar results in the temperature data of the five pixels of Fig. 9 (not shown). Lazarian & Draine (2000) predicted that spinning dust polarization should be no greater than 2 per cent at 20 GHz and become almost completely unpolarized above 40 GHz. If the anomalous component is due to spinning dust, then the dust-correlated polarization should be consistent with zero-polarization in the frequency range 40–61 GHz (*Q*–*V* bands), with the possibility of increasing polarization towards lower frequencies. Within the error bars, this is at least consistent with the behaviour observed in Fig. 9. Alternatively, Draine & Lazarian (1999) predict polarizations as high as 40 per cent in the 1–200 GHz range for emission from vibrating magnetic grains (although the actual polarization is not expected to be so high, given some level of beam depolarization and depolarization due to line-of-sight integration). Depending on the exact number of magnetic domains and the grains' aspect ratios, the magnetic grains' polarization may drop from its maximal value to zero almost anywhere within the same frequency range; the observed polarization as a function of frequency could have almost any behaviour (i.e. rising, falling, flat, or all three). Given the large uncertainties, we can only note here that the data plotted in Fig. 9 are not inconsistent with this behaviour.

5.5 Free–free

A simple fit to a power-law spectrum for the free–free emission in the all-sky analysis yields a free–free spectral index of $\beta_{\rm f} = -2.15 \pm 0.22$. In the latitude analysis and in the all-sky analysis, we find free–free emission is unpolarized ($\lesssim$1 per cent) over the sky. This result is confirmed in the pixel analysis, where over most of the sky free–free emission is unpolarized at the 1σ level, as reported in Table 3.

The upper limits in the distributions of the polarization fraction from simulations in the *K* band typically range between 5 and 15 per cent, apart from the regions around the Galactic poles that are essentially unconstrained. We find that in region 16 the detected free–free polarization is higher than all simulation results but still compatible with zero at the 2σ level when C-C errors are considered. In 16 out of the 48 pixel regions, we were able to put 2σ upper limits on fractional polarizations ranging from 10 per cent (in seven regions) to about 5 per cent (in nine regions). These upper limits are more stringent where the uncertainties are small, that is, where the free–free emission is higher, such as near the Galactic plane at longitudes between 200° and 300°. Some pixels (e.g. 14, 16, 17, 24, 31, 33, 40 and 43) do show significant cross-talk in the simulations. By comparing the simulations with the real data, we can isolate regions that we believe are not strongly affected by cross-talk and where the C-C errors are comparable or larger than the scatter in the simulations (therefore no significant bias). These are 4, 10, 11, 13,15, 19, 22, 23, 26, 27, 32, 34 and 41. Examples are shown in Fig. 10. The weighted average of these more reliable pixels is 0.0 ± 1.7 per cent, corresponding to an upper limit of 3.4 per cent (95 per cent confidence). The standard deviation in all 48 pixels is $\pm$5.5 per cent. We note that, unlike for dust, no regions exceed the simulation distributions at the 99th percentile and are individually significant (at $>2\sigma$).

6 CONCLUSIONS

We computed the C-C of the intensity and polarization *WMAP* data in different sky regions using templates for synchrotron, dust and free–free emission, plus a monopole-offset template. This technique is reliable because it takes into account the correlations between foregrounds, and because it requires no assumptions about the foregrounds' frequency behaviours. However, this study relies on the assumption of equal polarization angles for the three foregrounds and on the hypothesis of constant fractional polarization fraction in each of the the analysed sky regions. We derive the frequency dependence and polarization fraction for all three components in 48 different sky regions (delineated in HEALPix format at $N_{\rm side} = 2$ resolution).

This resolution is chosen as a compromise between (i) the assumption of uniform polarization fraction in any given sky region; and (ii) the need to average a large number of data points in order to minimize uncertainties.

The anomalous low-frequency emission correlated with thermal dust is clearly detected in intensity over the entire sky at the *WMAP* *K* and *Ka* bands. It is also found to be the dominant foreground at low Galactic latitude in the pixel analysis, between $b = -40°$ and 10°. The synchrotron spectral index obtained from the *K* and *Ka* bands is consistent with previous results, although small differences are

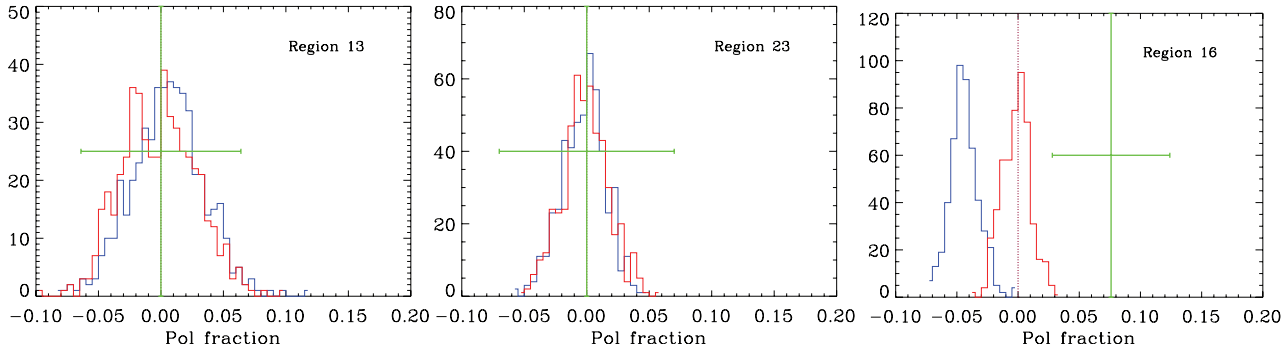

Figure 10. Histograms of the free–free polarization fraction at the K band for three regions, from 500 realizations at the K band, for the case with no dust polarization (red line) and with 3.5 per cent dust polarization (blue line). The input values are shown as the vertical dotted lines. The green line and error bar represent the best-fitting value and its 1σ uncertainty from the real data, respectively.

found between the polarization and temperature results in the pixel analysis. On the other hand, the values from the all-sky analysis ($\beta_s = -3.32 \pm 0.12$ for intensity and $\beta_s = -3.01 \pm 0.03$ for polarization) are compatible with an average value of $\beta_s \simeq -3$.

The polarization fraction of the synchrotron is constant in frequency and increases with latitude from 5 per cent near the Galactic plane to about 40 per cent in some regions at high latitudes; this is consistent with a depolarization effect due to integrating through high column densities in the plane. The average synchrotron fractional polarization at low latitudes ($|b| < 20^\circ$) is 8.6 ± 1.7 (stat) $\pm$ 0.5 (sys) per cent, while at high latitudes ($|b| > 20^\circ$), it is $19.3 \pm$ 0.8 (stat) $\pm$ 0.5 (sys) per cent with a standard deviation of ± 11.0 per cent. The robustness of these values was verified using Monte Carlo simulations.

Previous work has usually assumed that the anomalous dust-correlated emission in the K band is unpolarized. We find this assumption to be reasonable with most of the sky having polarization fractions less than 10 per cent. However, Monte Carlo simulations revealed that some pixels are likely to be affected by cross-talk, at up to the $\approx$5 per cent level. Taking an average of the significant ($>2\sigma$) regions led to a bias of $\approx$1.5 per cent in the simulations. The average polarization fraction, for the more reliable pixels, was 3.2 ± 0.9 (stat) $\pm$ 1.5 (sys) per cent. Given the average bias seen in the simulations (1.5 per cent), we do not claim a strong detection, while it is clear that the polarization fraction is less than 5 per cent at 95 per cent confidence. We found several pixels that appeared to have a significant detection of dust polarization at the K band while being robust in the simulations. Eight out of the 48 regions exceeded the 99th percentile of the distribution from simulations with no input foreground polarization, six of which are detected at above 2σ and display polarization fractions between 2.6 and 7.2 per cent, except for region 45 at $(l, b) \sim (46^\circ, -66^\circ)$, which was found to be polarized at 31.7 ± 11.7 per cent (2.7σ).

Free–free emission is found to be unpolarized over the entire sky with an upper limit on the fractional polarization of about 5 per cent in nine regions, and about 10 per cent in seven regions. Unlike for the dust, no regions were found to have a polarization fraction that exceeded the simulation distributions. Guided by simulations, we find an upper limit of 3.4 per cent (95 per cent confidence).

ACKNOWLEDGMENTS

This research was carried out at the Jet Propulsion Laboratory, California Institute of Technology, under a contract with the National Aeronautics and Space Administration and funded through the Director's Research and Development Fund Program. EP is an NSF-ADVANCE fellow (AST 06-49899) also supported by NASA grant NNX07AH59G and Planck subcontract 1290790. NM and EP were supported by JPL SURP award 1314616 for this work, and would like to thank Caltech for hospitality during this period. EP wishes to thank the Aspen Center for Physics where part of this work was carried out. CD acknowledges an STFC Advanced Fellowship and ERC grant under the FP7. JEV is supported by NSF AST 05-40882 and 08-38261 through the Caltech Submillimeter Observatory. The authors would like to thank Mark Halpern and Anthony Banday for useful conversations. We acknowledge the use of the LAMBDA. Support for the LAMBDA is provided by the NASA Office of Space Science. Some of the results in this paper have been derived using the HEALPix (Górski et al. 2005) package.

REFERENCES

Ali-Haïmoud Y., Hirata C. M., Dickinson C., 2009, MNRAS, 395, 1055
Banday A. J., Dickinson C., Davies R. D., Davis R. J., Górski K. M., 2003, MNRAS, 345, 897
Battistelli E. S., Rebolo R., Rubiño-Martín J. A., Hildebrandt S. R., Watson R. A., Gutiérrez C., Hoyland R. J., 2006, ApJ, 645, 141
Bennett C. L. et al., 2003, ApJS, 148, 97
Betoule M., Pierpaoli E., Delabrouille J., Le Jeune M., Cardoso J.-F., 2009, A&A, 503, 691
Brown M. L. et al., 2009, ApJ, 705, 978
Casassus S., Cabrera G. F., Förster F., Pearson T. J., Readhead A. C. S., Dickinson C., 2006, ApJ, 639, 951
Chiang H. C. et al., 2010, ApJ, 711, 1123
Cumberbatch D. T., Zuntz J., Kamfjord Eriksen H. K., Silk J., 2009, preprint (arXiv:0902.0039)
Davies R. D., Watson R. A., Gutierrez C. M., 1996, MNRAS, 278, 925
Davies R. D., Dickinson C., Banday A. J., Jaffe T. R., Górski K. M., Davis R. J., 2006, MNRAS, 370, 1125
de Oliveira-Costa A., Tegmark M., Gutierrez C. M., Jones A. W., Davies R. D., Lasenby A. N., Rebolo R., Watson R. A., 1999, ApJ, 527, L9
de Oliveira-Costa A. et al., 2002, ApJ, 567, 363
Delabrouille J., Cardoso J.-F., 2009, in Martínez V. J., Saar E., Martínez-González E., Pons-Bordería M.-J., eds, Data Analysis in Cosmology. Springer-Verlag, Berlin, p. 159
Dickinson C., Davies R. D., Davis R. J., 2003, MNRAS, 341, 369
Dickinson C. et al., 2004, MNRAS, 353, 732
Dickinson C. et al., 2009a, ApJ, 690, 1585
Dickinson C. et al., 2009b, ApJ, 705, 1607
Dickinson C. et al., 2010, MNRAS, 407, 2223
Dotson J. L., Davidson J., Dowell C. D., Schleuning D. A., Hildebrand R. H., 2000, ApJS, 128, 335
Dotson J. L., Vaillancourt J. E., Kirby L., Dowell C. D., Hildebrand R. H., Davidson J. A., 2010, ApJS, 186, 406

Draine B. T., Lazarian A., 1998a, ApJ, 494, L19
Draine B. T., Lazarian A., 1998b, ApJ, 508, 157
Draine B. T., Lazarian A., 1999, ApJ, 512, 740
Dunkley J. et al., 2009, ApJ, 701, 1804
Eriksen H. K., Jewell J. B., Dickinson C., Banday A. J., Górski K. M., Lawrence C. R., 2008, ApJ, 676, 10
Finkbeiner D. P., 2003, ApJS, 146, 407
Finkbeiner D. P., 2004, ApJ, 614, 186
Finkbeiner D. P., Davis M., Schlegel D. J., 1999, ApJ, 524, 867
Finkbeiner D. P., Langston G. I., Minter A. H., 2004, ApJ, 617, 350
Fosalba P., Lazarian A., Prunet S., Tauber J. A., 2002, ApJ, 564, 762
Gold B. et al., 2009, ApJS, 180, 265
Górski K. M., Hivon E., Banday A. J., Wandelt B. D., Hansen F. K., Reinecke M., Bartelmann M., 2005, ApJ, 622, 759
Haslam C. G. T., Klein U., Salter C. J., Stoffel H., Wilson W. E., Cleary M. N., Cooke D. J., Thomasson P., 1981, A&A, 100, 209
Haslam C. G. T., Stoffel H., Salter C. J., Wilson W. E., 1982, A&AS, 47, 1
Heiles C., 2000, AJ, 119, 923
Hildebrandt R., Kirby L., 2004, in Witt A. N., Clayton G. C., Draine B. T., eds, ASP Conf. Ser. Vol. 309, Astrophysics of Dust. Astron. Soc. Pac., San Francisco, p. 515
Hildebrand R. H., Dotson J. L., Dowell C. D., Schleuning D. A., Vaillancourt J. E., 1999, ApJ, 516, 834
Hildebrandt R., Rebolo R., Rubiño-Martín J. A., Watson R. A., Gutiérrez C. M., Hoyland R. J., Battistelli E. S., 2007, MNRAS, 382, 594
Hinshaw G. et al., 2007, ApJS, 170, 288
Hinshaw G. et al., 2009, ApJS, 180, 225
Jonas J. L., Baart E. E., Nicolson G. D., 1998, MNRAS, 297, 977
Jones W. C. et al., 2006, ApJ, 647, 823
Kogut A. et al., 1996, ApJ, 464, L5
Kogut A. et al., 2007, ApJ, 665, 355
Lazarian A., 2003, J. Quant. Spectrosc. Radiat. Transfer, 79, 881
Lazarian A., 2007, J. Quant. Spectrosc. Radiat. Transfer, 106, 225
Lazarian A., Draine B. T., 2000, ApJ, 536, 15
Lazarian A., Finkbeiner D., 2003, New Astron. Rev., 47, 1107
Leach S. M. et al., 2008, A&A, 491, 597
López-Caraballo C. H., Rubiño-Martín J. A., Rebolo R., Génova-Santos R., 2011, ApJ, 729, 25
Martin P. G., 2007, in Miville-Deschenes M.-A., Boulanger G., eds, EAS Publ. Ser. Vol. 23, Sky Polarization at Far Infrared to Radio Wavelengths: The Galactic Screen before the Cosmic Microwave Background. EDP Sciences, Les Ulis, p. 165
Mason B. S., Robishaw T., Heiles C., Finkbeiner D., Dickinson C., 2009, ApJ, 697, 1187
Mather J. C., Fixsen D. J., Shafer R. A., Mosier C., Wilkinson D. T., 1999, ApJ, 512, 511
Matthews B. C., McPhee C., Fissel L., Curran R., 2009, ApJS, 182, 143
Miville-Deschênes M. A., Ysard N., Lavabre A., Ponthieu N., Macías-Pérez J. F., Aumont J., Bernard J. P., 2008, A&A, 490, 1093
Nolta M. et al., 2009, ApJS, 180, 296
Page L. et al., 2007, ApJS, 170, 335
Planck Collaboration et al., 2011, A&A, preprint (arXiv:1101.2031)
Platania P., Burigana C., Maino D., Caserini E., Bersanelli M., Cappellini B., Mennella A., 2003, A&A, 410, 847
Ponthieu N. et al., 2005, A&A, 444, 327
Pryke C. et al., 2009, ApJ, 692, 1247
Reich P., Reich W., 1986, A&AS, 63, 205
Reichardt C. L. et al., 2009, ApJ, 694, 1200
Rybicki G. B., Lightman A. P., 1979, Radiative Processes in Astrophysics. Wiley Interscience, New York
Scaife A. M. M. et al., 2009, MNRAS, 400, 1394
Schlegel D. J., Finkbeiner D. P., Davis M., 1998, ApJ, 500, 525
Sievers J. L. et al., 2009, ApJ, preprint (arXiv:0901.4540)
Simmons J. F. L., Stewart B. G., 1985, A&A, 142, 100
Vaillancourt J. E., 2006, PASP, 118, 1340
Vaillancourt J. E. et al., 2008, ApJ, 679, L25
Watson R. A., Rebolo R., Rubiño-Martin J. A., Hildebrandt S., Gutièrrez C. M., Fernàndez-Cerezo S., Hoyland R. J., Battistelli E. S., 2005, ApJ, 624, L89
Wolleben M., Landecker T. L., Reich W., Wielebinski R., 2006, A&A, 448, 411

APPENDIX A: COMPLETE TABLES OF CROSS-CORRELATION COEFFICIENTS

Here, we report the C-C coefficients for dust, synchrotron and free–free emission resulting from our analysis.

Table A1. Full fit temperature coefficients for dust emission in all 48 pixel regions, with associated 1σ errors (in μK μK_{FDS}^{-1}).

Pixel	*K* band	*Ka* band	*Q* band	*V* band	*W* band
			Dust temperature C-C coefficients		
1	12.8 ± 2.7	9.2 ± 2.9	8.4 ± 3.2	7.6 ± 2.8	7.2 ± 3.8
2	-2.9 ± 5.2	-10.4 ± 5.6	-10.7 ± 6	-11.5 ± 5.9	-10 ± 6.8
3	8.2 ± 2.8	2.7 ± 2.8	0.7 ± 2.8	0.8 ± 3.2	0.3 ± 3.4
4	6.9 ± 2.5	1.6 ± 2.5	-0.4 ± 2.6	-0.6 ± 2.7	0.6 ± 3.4
5	8.2 ± 0.6	2.4 ± 0.7	1.1 ± 0.7	0.7 ± 0.7	1 ± 0.7
6	15.4 ± 2.5	8.5 ± 2.7	6.5 ± 2.6	5.7 ± 2.7	4.8 ± 3
7	5 ± 0.5	1.7 ± 0.5	1 ± 0.5	0.8 ± 0.7	1.1 ± 0.6
8	8.4 ± 1.2	4.1 ± 1.3	2.9 ± 1.4	2.4 ± 1.3	2.3 ± 1.4
9	3.1 ± 3	-0.6 ± 3.1	-1.9 ± 3.2	-2.2 ± 3.5	-1.6 ± 3.4
10	7.8 ± 1.7	2.8 ± 1.8	1.4 ± 2	1.1 ± 2.1	0.7 ± 2
11	8.3 ± 1.2	3 ± 1.2	2 ± 1.3	1.7 ± 1.3	1.7 ± 1.3
12	9.5 ± 0.9	1.9 ± 1	0.2 ± 0.9	-1 ± 1.1	-0.5 ± 1.3
13	8.3 ± 0.6	3.2 ± 0.6	2.2 ± 0.7	1.5 ± 0.7	1.7 ± 0.7
14	5.3 ± 0.4	1.5 ± 0.5	0.6 ± 0.5	0.3 ± 0.5	0.7 ± 0.5
15	6.8 ± 0.2	2.3 ± 0.2	1.3 ± 0.2	0.8 ± 0.3	1.1 ± 0.2
16	4.8 ± 0.3	0.7 ± 0.3	-0.2 ± 0.3	-0.6 ± 0.3	-0.2 ± 0.4
17	7.3 ± 0.3	3.3 ± 0.3	2.2 ± 0.3	1.6 ± 0.3	1.9 ± 0.4
18	9.5 ± 0.7	5.5 ± 0.7	4.7 ± 0.7	4 ± 0.7	4.1 ± 0.7
19	3.7 ± 0.6	-0.1 ± 0.6	-0.7 ± 0.6	-0.9 ± 0.7	-0.1 ± 0.6
20	8 ± 0.8	2.1 ± 0.9	0.9 ± 0.9	0.4 ± 0.9	0.7 ± 1.1
21	5.2 ± 0.7	0.6 ± 0.8	-0.4 ± 0.8	-0.7 ± 0.7	-0.7 ± 0.8
22	4.3 ± 0.4	0.6 ± 0.4	-0.1 ± 0.4	-0.4 ± 0.5	0.1 ± 0.4
23	5.3 ± 0.4	0.9 ± 0.4	-0.2 ± 0.4	-0.7 ± 0.5	-0.3 ± 0.5
24	6.5 ± 0.4	2.7 ± 0.4	1.8 ± 0.4	1.4 ± 0.4	1.9 ± 0.5
25	5.9 ± 0.3	2.3 ± 0.3	1.4 ± 0.4	0.9 ± 0.3	1.3 ± 0.4
26	5.9 ± 0.6	0.9 ± 0.6	-0.2 ± 0.7	-0.7 ± 0.7	-0.2 ± 0.8
27	5.6 ± 0.4	1.7 ± 0.4	0.9 ± 0.4	0.5 ± 0.5	1 ± 0.5
28	9 ± 4.1	0.9 ± 4.2	0.4 ± 4.8	-1.3 ± 4.9	0.2 ± 5.2
29	11.5 ± 0.6	4.9 ± 0.6	3.5 ± 0.7	2.4 ± 0.8	2.5 ± 0.8
30	8.3 ± 0.6	3.3 ± 0.6	2.1 ± 0.7	1.4 ± 0.6	1.8 ± 0.6
31	11.8 ± 0.5	6.5 ± 0.5	5 ± 0.6	4 ± 0.6	3.8 ± 0.6
32	7.7 ± 0.4	2.7 ± 0.4	1.5 ± 0.4	0.8 ± 0.5	1.2 ± 0.5
33	6.1 ± 0.2	2.8 ± 0.2	1.9 ± 0.2	1.5 ± 0.2	1.7 ± 0.2
34	4.9 ± 0.2	1.5 ± 0.3	0.9 ± 0.3	0.7 ± 0.3	1.1 ± 0.3
35	5.9 ± 0.6	1.5 ± 0.6	0.4 ± 0.7	-0.1 ± 0.6	0.3 ± 0.8
36	7.1 ± 0.3	2.8 ± 0.3	1.7 ± 0.4	1.1 ± 0.4	1.3 ± 0.4
37	4.4 ± 1.4	-0.5 ± 1.5	-1.3 ± 1.7	-2.1 ± 1.4	-1.7 ± 1.6
38	8.3 ± 1	3.3 ± 1	2.1 ± 1.1	1.1 ± 1.1	1.4 ± 1.3
39	5.4 ± 0.8	0.7 ± 0.8	0 ± 0.9	-0.6 ± 1	-0.1 ± 0.9
40	7 ± 0.3	2.1 ± 0.3	0.8 ± 0.3	0 ± 0.3	0.2 ± 0.4
41	8.7 ± 0.5	3.1 ± 0.5	1.8 ± 0.5	1 ± 0.5	1.3 ± 0.5
42	7.3 ± 2.3	3.8 ± 2.5	2.7 ± 2.6	2.4 ± 2.6	2.5 ± 2.4
43	9 ± 0.6	4.2 ± 0.6	2.9 ± 0.7	1.9 ± 0.6	2.1 ± 0.6
44	6 ± 2	0.9 ± 2	0.4 ± 2.3	-0.5 ± 2.5	0.3 ± 2.7
45	8.5 ± 2.3	4.3 ± 2.5	1.9 ± 2.6	1.9 ± 2.7	1.4 ± 3.2
46	1.2 ± 1.2	-3.4 ± 1.3	-4.4 ± 1.3	-4.4 ± 1.2	-3.3 ± 1.5
47	16.2 ± 3.2	8.8 ± 3.2	6.6 ± 3.6	6.3 ± 3.9	5.9 ± 3.9
48	3.3 ± 5.5	-1.8 ± 5.9	-3.1 ± 6.2	-5.7 ± 6.6	-5.4 ± 5.9

Table A2. Full fit coefficients for polarized dust emission in all 48 pixel regions, with associated 1σ errors (in μK μK^{-1}_{FDS}).

Pixel	*K* band	*Ka* band	*Q* band	*V* band	*W* band
			Dust polarization C-C coefficients		
1	-1.1 ± 0.7	-0.4 ± 0.7	0.3 ± 0.6	-0.3 ± 0.8	-0.9 ± 1
2	-1.2 ± 1.5	0.1 ± 1.5	-0.3 ± 1.4	-0.3 ± 1.7	0.3 ± 2.1
3	0.4 ± 0.8	0.3 ± 0.8	0.2 ± 0.8	-0.6 ± 1	0.1 ± 1.1
4	-0.9 ± 0.8	0.2 ± 0.8	-0.2 ± 0.9	-0.4 ± 1	0.4 ± 1.2
5	0.6 ± 0.2	0.2 ± 0.2	0.3 ± 0.2	0.1 ± 0.2	0 ± 0.3
6	1.6 ± 0.7	0 ± 0.7	0.4 ± 0.6	-0.1 ± 0.8	-0.4 ± 1
7	-0.1 ± 0.1	0.1 ± 0.1	0 ± 0.1	0 ± 0.2	0 ± 0.2
8	-0.5 ± 0.3	-0.2 ± 0.3	0 ± 0.3	0.2 ± 0.4	0 ± 0.4
9	0 ± 0.9	0.1 ± 0.9	0.1 ± 0.8	0.3 ± 1	-0.2 ± 1.2
10	-0.3 ± 0.5	-0.2 ± 0.5	0.1 ± 0.5	0.4 ± 0.6	0.8 ± 0.7
11	-1.3 ± 0.4	0 ± 0.4	-0.1 ± 0.4	-0.1 ± 0.5	-0.3 ± 0.6
12	-0.4 ± 0.3	-0.3 ± 0.3	0 ± 0.3	0.1 ± 0.3	0.2 ± 0.4
13	-0.1 ± 0.2	0.3 ± 0.2	0 ± 0.2	0 ± 0.3	-0.1 ± 0.3
14	-1.6 ± 0.1	-0.4 ± 0.1	-0.2 ± 0.1	-0.1 ± 0.1	0 ± 0.1
15	-0.1 ± 0	0 ± 0	0 ± 0	0 ± 0	0 ± 0.1
16	-0.3 ± 0.1	0 ± 0.1	0 ± 0.1	0 ± 0.1	0 ± 0.1
17	0.2 ± 0.1	0 ± 0.1	0.1 ± 0.1	0 ± 0.1	-0.1 ± 0.1
18	-0.2 ± 0.2	0 ± 0.2	-0.1 ± 0.2	0 ± 0.2	-0.3 ± 0.3
19	-0.3 ± 0.2	0.1 ± 0.2	-0.1 ± 0.2	0 ± 0.2	0.2 ± 0.2
20	-0.1 ± 0.3	-0.2 ± 0.3	0.1 ± 0.3	-0.1 ± 0.4	0.2 ± 0.4
21	0.4 ± 0.3	0.4 ± 0.3	0.1 ± 0.3	0.1 ± 0.4	-0.2 ± 0.5
22	0 ± 0.1	0 ± 0.1	0 ± 0.1	0 ± 0.1	0 ± 0.2
23	0.3 ± 0.1	0.1 ± 0.1	0.1 ± 0.1	0 ± 0.1	-0.1 ± 0.2
24	0.2 ± 0.1	0.2 ± 0.1	0.1 ± 0.1	0.2 ± 0.2	-0.3 ± 0.2
25	0.2 ± 0.1	0.1 ± 0.1	0 ± 0.1	0 ± 0.1	0 ± 0.2
26	-0.1 ± 0.2	-0.1 ± 0.2	0 ± 0.2	0 ± 0.2	0 ± 0.2
27	0.2 ± 0.1	0.1 ± 0.1	0.1 ± 0.1	0 ± 0.1	0.1 ± 0.1
28	-0.8 ± 1.8	0.4 ± 1.9	-1.6 ± 1.8	-0.1 ± 2.2	-1.9 ± 2.6
29	-0.8 ± 0.2	-0.2 ± 0.2	-0.1 ± 0.2	-0.1 ± 0.2	0 ± 0.2
30	-0.2 ± 0.2	-0.1 ± 0.2	0.1 ± 0.2	0 ± 0.2	0 ± 0.3
31	0 ± 0.1	0 ± 0.1	0.1 ± 0.1	0 ± 0.1	0 ± 0.2
32	0.1 ± 0.1	-0.1 ± 0.1	0 ± 0.1	0.1 ± 0.1	0 ± 0.2
33	-0.1 ± 0.1	0 ± 0.1	0.1 ± 0.1	0 ± 0.1	0 ± 0.1
34	0.2 ± 0.1	0.1 ± 0.1	0 ± 0.1	0 ± 0.1	0 ± 0.1
35	0.2 ± 0.1	0 ± 0.1	0 ± 0.1	0.1 ± 0.1	-0.1 ± 0.1
36	-0.1 ± 0.1	0 ± 0.1	0.1 ± 0.1	0 ± 0.1	0 ± 0.1
37	-0.7 ± 0.4	-0.2 ± 0.4	-0.4 ± 0.4	0.1 ± 0.5	0.1 ± 0.6
38	0.1 ± 0.3	-0.1 ± 0.3	0.1 ± 0.3	0 ± 0.3	0.1 ± 0.4
39	0.2 ± 0.3	-0.1 ± 0.3	-0.1 ± 0.3	-0.1 ± 0.3	0 ± 0.4
40	0 ± 0.1	0 ± 0.1	0 ± 0.1	0 ± 0.1	0 ± 0.1
41	0 ± 0.2	0 ± 0.2	0.1 ± 0.2	0 ± 0.2	0.2 ± 0.2
42	-1.1 ± 0.7	-0.2 ± 0.7	0.1 ± 0.6	0 ± 0.8	0.1 ± 1
43	0 ± 0.1	-0.1 ± 0.1	0 ± 0.1	0 ± 0.1	0 ± 0.1
44	-0.9 ± 0.5	-0.2 ± 0.5	-0.5 ± 0.5	0.2 ± 0.6	0.1 ± 0.8
45	2.7 ± 0.7	0 ± 0.7	0.4 ± 0.7	0 ± 0.9	0.1 ± 1
46	0.5 ± 0.3	0 ± 0.3	0.2 ± 0.3	0.2 ± 0.4	0 ± 0.5
47	-0.8 ± 0.8	-0.2 ± 0.8	-0.1 ± 0.7	0.2 ± 0.9	-0.5 ± 1.1
48	-0.7 ± 1.4	-0.5 ± 1.5	-0.9 ± 1.3	1 ± 1.7	-1.3 ± 2

Table A3. Full fit temperature coefficients for synchrotron emission in all 48 pixel regions, with associated 1σ errors (in μK $K^{-1}_{408\,MHz}$).

Pixel	*K* band	*Ka* band	*Q* band	*V* band	*W* band
			Synchrotron temperature C-C coefficients		
1	5.9 ± 0.6	2.1 ± 0.6	1.3 ± 0.7	0.5 ± 0.7	0.4 ± 0.6
2	-4.4 ± 2	-6.9 ± 2.2	-7 ± 2.2	-6.8 ± 2.4	-6.2 ± 2.2
3	4.2 ± 2.5	1.4 ± 2.6	-0.1 ± 2.8	-0.5 ± 3.2	-0.3 ± 3.4
4	8.4 ± 0.9	4.4 ± 0.9	3.4 ± 0.9	2.8 ± 1	1.9 ± 1.3
5	6 ± 0.4	3 ± 0.4	2.3 ± 0.4	1.9 ± 0.4	1.5 ± 0.5
6	0.6 ± 1.4	-1.2 ± 1.6	-1.7 ± 1.5	-2 ± 1.8	-1.7 ± 1.9
7	4.8 ± 1.2	2 ± 1.3	1.5 ± 1.5	0.6 ± 1.6	0.7 ± 1.6
8	2.3 ± 1	-1.9 ± 1.1	-2.8 ± 1.2	-3.1 ± 1.2	-3 ± 1
9	4.2 ± 1.8	0.5 ± 1.9	-0.1 ± 2	-0.5 ± 2	-0.9 ± 2.4
10	6.5 ± 1.7	3.4 ± 1.8	2.1 ± 1.8	1.4 ± 1.9	1.2 ± 1.8
11	5.4 ± 1	1.5 ± 1	0.2 ± 1	-0.1 ± 1.2	-0.4 ± 1
12	5.9 ± 1	2.9 ± 1	2 ± 1	1.5 ± 1.2	1 ± 1.3
13	5.1 ± 1.1	0.2 ± 1.1	-1.1 ± 1.2	-1.6 ± 1.1	-1.5 ± 1.3
14	7.2 ± 0.3	3.4 ± 0.3	2.5 ± 0.3	1.9 ± 0.4	1.4 ± 0.4
15	-1.6 ± 0.9	-4.2 ± 0.9	-4.7 ± 1	-4.9 ± 1.1	-4.2 ± 1.1
16	12.9 ± 0.8	7.9 ± 0.9	6.9 ± 0.9	5.8 ± 0.9	5.1 ± 1.2
17	5.5 ± 0.9	2.3 ± 1	1.7 ± 1.1	1.4 ± 1.2	0.8 ± 1
18	1.2 ± 1.4	-1.2 ± 1.4	-1.7 ± 1.4	-1.8 ± 1.4	-1.9 ± 1.6
19	3 ± 1.1	-0.9 ± 1.1	-1.5 ± 1.2	-1.8 ± 1.4	-1.7 ± 1.2
20	9.1 ± 0.3	3.9 ± 0.3	2.6 ± 0.3	1.6 ± 0.3	1.1 ± 0.4
21	7 ± 0.7	3.1 ± 0.7	2.2 ± 0.8	1.1 ± 0.8	1.1 ± 1
22	8.3 ± 1.2	6 ± 1.2	5.1 ± 1.3	4.3 ± 1.2	3.5 ± 1.4
23	9.9 ± 1.6	5.3 ± 1.7	3.8 ± 1.8	3.1 ± 1.9	2.4 ± 2.3
24	3.8 ± 1.8	1.8 ± 2	1.8 ± 2.2	1.3 ± 1.9	0.3 ± 2.5
25	-3.7 ± 0.9	-7.6 ± 0.9	-8.6 ± 0.9	-8.9 ± 1.1	-7.8 ± 1.2
26	2.6 ± 1.7	3.1 ± 1.9	3.4 ± 1.9	3.4 ± 2	3.4 ± 2.4
27	10.4 ± 0.8	6.1 ± 0.9	5 ± 0.9	3.8 ± 0.9	2.9 ± 1
28	11.3 ± 2.2	6.9 ± 2.4	5.1 ± 2.6	4.1 ± 2.6	3 ± 2.6
29	7.2 ± 0.6	1.7 ± 0.6	0.3 ± 0.7	-0.7 ± 0.7	-0.6 ± 0.7
30	4.2 ± 0.6	0.9 ± 0.6	0.2 ± 0.7	-0.2 ± 0.6	-0.3 ± 0.7
31	-0.6 ± 1.1	-3.5 ± 1.2	-3.8 ± 1.3	-4 ± 1.2	-3.9 ± 1.3
32	7.2 ± 1	3.9 ± 1.1	3 ± 1.1	2.3 ± 1.3	1.7 ± 1.3
33	4.6 ± 0.9	0.4 ± 0.9	-0.4 ± 0.9	-1 ± 0.9	-1.3 ± 1
34	14.6 ± 1.3	10.2 ± 1.3	8.7 ± 1.4	7.1 ± 1.6	6 ± 1.7
35	0 ± 1.6	-2.7 ± 1.7	-3.1 ± 1.6	-3 ± 2	-2.8 ± 1.8
36	4.4 ± 0.5	-0.1 ± 0.5	-1.2 ± 0.6	-1.9 ± 0.7	-1.8 ± 0.6
37	7.1 ± 1.3	3.1 ± 1.4	1.9 ± 1.3	2 ± 1.3	1.1 ± 1.4
38	-1.2 ± 1.1	-3.4 ± 1.1	-3.4 ± 1.2	-3.5 ± 1.1	-3 ± 1.1
39	5.8 ± 2	2 ± 2.1	0.7 ± 2.2	-0.4 ± 2.3	0.3 ± 2.8
40	-6.6 ± 1.2	-10.7 ± 1.3	-11.3 ± 1.3	-11.3 ± 1.3	-9.5 ± 1.5
41	-3 ± 1.5	-5 ± 1.5	-5.8 ± 1.7	-6.1 ± 1.6	-5.4 ± 1.8
42	2.4 ± 2.2	-0.3 ± 2.3	-1 ± 2.2	-1.4 ± 2.7	-1.5 ± 2.9
43	-0.1 ± 1.3	-2.3 ± 1.4	-2.9 ± 1.5	-3.2 ± 1.4	-2.6 ± 1.8
44	7.7 ± 1	2.9 ± 1	1.3 ± 1	0.6 ± 1.1	0.4 ± 1.1
45	6.1 ± 1.5	3.1 ± 1.5	2.6 ± 1.5	2.2 ± 1.8	2 ± 1.6
46	12.7 ± 1.8	8.9 ± 1.8	8 ± 2.1	7.7 ± 2	6.1 ± 1.9
47	5.6 ± 2	0.1 ± 2.1	-0.9 ± 2.4	-2 ± 2.2	-1.8 ± 2.7
48	-1.4 ± 1.8	-4 ± 2	-4.4 ± 1.9	-4.8 ± 2.2	-3.9 ± 2.4

Table A4. Full fit coefficients for polarized synchrotron emission in all 48 pixel regions, with associated 1σ errors (in $\mu K\, K^{-1}_{408\,MHz}$).

Pixel	*K* band	*Ka* band	*Q* band	*V* band	*W* band
	Synchrotron polarization C-C coefficients				
1	2.4 ± 0.2	0.8 ± 0.2	0.4 ± 0.1	0 ± 0.2	0.3 ± 0.2
2	0.6 ± 0.4	0.2 ± 0.4	0.2 ± 0.4	0 ± 0.5	-0.4 ± 0.6
3	1.9 ± 0.7	0.4 ± 0.7	0.3 ± 0.7	0.7 ± 0.8	0.2 ± 1
4	2 ± 0.2	0.6 ± 0.2	0.2 ± 0.2	-0.1 ± 0.3	-0.2 ± 0.3
5	1.6 ± 0.1	0.5 ± 0.1	0.3 ± 0.1	0.1 ± 0.1	0.1 ± 0.1
6	0.5 ± 0.3	0.4 ± 0.3	0 ± 0.3	0 ± 0.3	0.1 ± 0.4
7	0.9 ± 0.3	0.2 ± 0.3	-0.1 ± 0.3	0 ± 0.3	0.2 ± 0.4
8	1 ± 0.2	0.2 ± 0.2	0 ± 0.2	-0.1 ± 0.3	0.1 ± 0.3
9	0.7 ± 0.5	0.5 ± 0.5	0.3 ± 0.5	0.1 ± 0.6	0.3 ± 0.8
10	1.2 ± 0.4	0 ± 0.4	0 ± 0.4	0 ± 0.4	0 ± 0.5
11	1.2 ± 0.3	0 ± 0.3	-0.1 ± 0.3	0.2 ± 0.3	0.2 ± 0.4
12	1.3 ± 0.3	0.6 ± 0.3	0.2 ± 0.3	0.1 ± 0.3	0.1 ± 0.4
13	2.3 ± 0.4	0.7 ± 0.4	-0.1 ± 0.4	-0.3 ± 0.5	0.3 ± 0.6
14	1.7 ± 0.1	0.5 ± 0.1	0.3 ± 0.1	0.1 ± 0.1	0 ± 0.1
15	1.8 ± 0.2	0.6 ± 0.2	0.2 ± 0.1	0 ± 0.2	-0.1 ± 0.2
16	2.6 ± 0.2	0.7 ± 0.2	0.3 ± 0.2	0.1 ± 0.2	0.2 ± 0.3
17	1.6 ± 0.3	0.5 ± 0.3	-0.1 ± 0.3	0 ± 0.3	0.1 ± 0.4
18	1 ± 0.3	0 ± 0.3	0.4 ± 0.3	0 ± 0.4	0.3 ± 0.5
19	1.1 ± 0.3	0.2 ± 0.3	0.2 ± 0.3	0 ± 0.4	-0.1 ± 0.4
20	1.3 ± 0.1	0.3 ± 0.1	0.1 ± 0.1	0 ± 0.1	0 ± 0.1
21	-0.1 ± 0.3	0.1 ± 0.3	0 ± 0.3	0 ± 0.4	0.4 ± 0.5
22	0.5 ± 0.3	0 ± 0.3	-0.1 ± 0.2	0 ± 0.3	-0.1 ± 0.4
23	1.1 ± 0.5	0.3 ± 0.5	0.1 ± 0.5	0.3 ± 0.6	0.3 ± 0.8
24	1.7 ± 0.6	0.2 ± 0.6	0.4 ± 0.6	-0.6 ± 0.8	0.8 ± 0.9
25	1.5 ± 0.3	0.1 ± 0.3	0.2 ± 0.3	0.3 ± 0.3	0 ± 0.4
26	0.6 ± 0.4	0.3 ± 0.4	0.1 ± 0.4	0.1 ± 0.5	0.1 ± 0.6
27	1 ± 0.2	0.2 ± 0.2	-0.1 ± 0.2	-0.1 ± 0.3	0 ± 0.3
28	0.5 ± 1.1	-0.2 ± 1.1	1 ± 1	0.2 ± 1.3	1 ± 1.5
29	1.4 ± 0.2	0.5 ± 0.2	0.2 ± 0.2	0 ± 0.2	0 ± 0.2
30	0.3 ± 0.1	0.1 ± 0.2	0 ± 0.2	0 ± 0.2	0 ± 0.2
31	1.3 ± 0.2	0.3 ± 0.2	0.1 ± 0.2	-0.1 ± 0.3	0.1 ± 0.3
32	2.6 ± 0.2	1 ± 0.2	0.4 ± 0.2	-0.1 ± 0.3	-0.2 ± 0.3
33	2.5 ± 0.3	0.8 ± 0.3	0.2 ± 0.3	0.2 ± 0.4	-0.4 ± 0.5
34	1 ± 0.3	-0.1 ± 0.3	0.1 ± 0.3	-0.1 ± 0.4	-0.1 ± 0.5
35	0.6 ± 0.3	0.3 ± 0.3	0 ± 0.3	-0.2 ± 0.4	0.5 ± 0.5
36	1.2 ± 0.1	0.4 ± 0.1	0.2 ± 0.1	0.1 ± 0.1	-0.1 ± 0.2
37	1.5 ± 0.4	0.3 ± 0.4	0.3 ± 0.4	-0.1 ± 0.4	-0.3 ± 0.5
38	0.5 ± 0.3	0.6 ± 0.3	0 ± 0.3	-0.1 ± 0.4	0 ± 0.4
39	0.7 ± 0.6	0.3 ± 0.7	0.1 ± 0.6	0.1 ± 0.8	-0.1 ± 0.9
40	0.5 ± 0.3	0.3 ± 0.3	0.1 ± 0.3	0 ± 0.3	0 ± 0.4
41	0.3 ± 0.4	0.1 ± 0.4	-0.1 ± 0.4	0 ± 0.5	-0.2 ± 0.6
42	1.8 ± 0.5	0.4 ± 0.5	0.3 ± 0.4	0.1 ± 0.6	0.1 ± 0.7
43	1 ± 0.2	0.5 ± 0.2	0.1 ± 0.2	-0.1 ± 0.2	-0.1 ± 0.3
44	3 ± 0.2	0.9 ± 0.2	0.6 ± 0.2	-0.1 ± 0.3	0 ± 0.3
45	1.5 ± 0.4	0.9 ± 0.4	0 ± 0.4	0 ± 0.5	0.1 ± 0.6
46	0.1 ± 0.5	0 ± 0.5	0.2 ± 0.5	-0.1 ± 0.6	-0.6 ± 0.7
47	0.8 ± 0.4	0.4 ± 0.4	0.7 ± 0.4	0.2 ± 0.5	-0.1 ± 0.6
48	2 ± 0.4	0.7 ± 0.4	0.4 ± 0.3	-0.2 ± 0.4	0 ± 0.5

Table A5. Full fit temperature coefficients for free–free emission in all 48 pixel regions, with associated 1σ errors (in $\mu K\, R^{-1}$).

Pixel	*K* band	*Ka* band	*Q* band	*V* band	*W* band
	Free–free temperature C-C coefficients				
1	-59.9 ± 23.9	-44.7 ± 25.1	-39 ± 24.4	-32 ± 29.6	-27.1 ± 33.4
2	67.2 ± 21.7	77.6 ± 22.8	80.9 ± 26.1	79 ± 27.6	62.8 ± 23.5
3	-44.5 ± 11.3	-40.6 ± 11.6	-42.1 ± 11.5	-41.1 ± 12.3	-33.3 ± 11.8
4	22.1 ± 3.5	12.8 ± 3.6	9.6 ± 4	5.7 ± 4.6	2.5 ± 4.8
5	12.1 ± 10.1	8.4 ± 11.1	10 ± 10.5	4.9 ± 12.5	3.4 ± 11.3
6	-8.1 ± 8.5	-10.4 ± 9.2	-10.2 ± 9.7	-11.6 ± 9.7	-9.2 ± 11.5
7	17.3 ± 7.3	10.4 ± 8.1	7.1 ± 8.4	5.7 ± 8.7	4.6 ± 10.3
8	-10.3 ± 13.1	-10.7 ± 14.2	-10 ± 15.1	-9.9 ± 14.2	-5.6 ± 14.1
9	-3.3 ± 5.4	-7.4 ± 5.8	-8.1 ± 5.7	-9.9 ± 6.1	-8 ± 6.7
10	19.6 ± 4.8	16.6 ± 5.1	15.3 ± 5.3	11.7 ± 5.9	8.7 ± 5.5
11	19.2 ± 3.3	16.8 ± 3.4	15.8 ± 3.9	13.7 ± 3.9	12.6 ± 3.4
12	6.4 ± 4.6	0.4 ± 5	-2.3 ± 5.4	-6.2 ± 4.9	-5.7 ± 5.5
13	22.6 ± 2.1	14.3 ± 2.2	11.8 ± 2.5	7.8 ± 2.2	6.3 ± 2.5
14	0 ± 3.7	-3.2 ± 3.8	-4 ± 4.3	-5.2 ± 4.2	-5.4 ± 4
15	15.2 ± 1.4	10.3 ± 1.5	8.6 ± 1.5	6.7 ± 1.5	5.7 ± 1.8
16	7.2 ± 1.7	3.1 ± 1.7	1.7 ± 1.8	-0.3 ± 1.8	-0.8 ± 2
17	-0.4 ± 1.9	-3.3 ± 2	-4.4 ± 2.2	-5.5 ± 2	-5 ± 2
18	3.1 ± 3.2	-1.1 ± 3.5	-3.2 ± 3.8	-3.6 ± 3.8	-3.6 ± 4
19	9.8 ± 0.6	5.6 ± 0.6	4 ± 0.7	2.2 ± 0.7	1.2 ± 0.6
20	-1.8 ± 1.4	-2.6 ± 1.5	-3.4 ± 1.6	-3.9 ± 1.8	-3.9 ± 1.8
21	18.6 ± 4.2	6.7 ± 4.3	2.1 ± 5	1.2 ± 4.8	-2 ± 5.3
22	11.7 ± 1.1	4.2 ± 1.2	1.7 ± 1.2	-0.5 ± 1.2	-1.2 ± 1.6
23	13.9 ± 1.8	8.9 ± 1.9	7.5 ± 2	5.4 ± 2.2	4.5 ± 2.6
24	7.5 ± 2.9	0.2 ± 3.2	-3 ± 3.1	-6 ± 3.4	-5.7 ± 3.3
25	9.8 ± 1.4	6.8 ± 1.4	5.9 ± 1.5	4.8 ± 1.5	3.5 ± 2
26	10.3 ± 0.6	5.3 ± 0.6	3.6 ± 0.6	1.8 ± 0.7	0.9 ± 0.7
27	3.6 ± 0.8	0 ± 0.8	-1.7 ± 0.9	-2.9 ± 0.9	-2.6 ± 0.9
28	-14.8 ± 4	-14.9 ± 4.1	-14.7 ± 4.8	-12.9 ± 4.9	-10.8 ± 5.3
29	-1.1 ± 2.5	-1.9 ± 2.6	-2 ± 2.8	-2.6 ± 2.6	-3.6 ± 3.2
30	-1.6 ± 5.1	-0.7 ± 5.4	-0.5 ± 5.9	-2.2 ± 5.8	-3 ± 5.9
31	8.2 ± 1.1	2.6 ± 1.2	0.7 ± 1.3	-1 ± 1.3	-1.5 ± 1.4
32	12.2 ± 1.6	6.2 ± 1.7	3.7 ± 1.8	1.8 ± 1.9	0.9 ± 1.9
33	7.7 ± 0.6	4.4 ± 0.7	3.3 ± 0.7	2 ± 0.7	1.2 ± 0.8
34	2.6 ± 0.5	0 ± 0.5	-1.2 ± 0.6	-2.2 ± 0.6	-2.4 ± 0.5
35	8 ± 0.4	4.6 ± 0.4	3.4 ± 0.5	1.9 ± 0.5	1.3 ± 0.5
36	-3.5 ± 1.6	-4.7 ± 1.7	-4.7 ± 1.7	-5 ± 1.7	-4.4 ± 2
37	14.7 ± 9.4	17.7 ± 9.6	20.5 ± 10.3	16.5 ± 10.8	20.5 ± 10.9
38	14.7 ± 6.2	13.1 ± 6.7	11.3 ± 6.6	9.2 ± 8.1	6.9 ± 7.7
39	21.1 ± 7.9	18.7 ± 8	20.3 ± 8.6	18.6 ± 9.8	11.7 ± 8.9
40	14.1 ± 3.1	8.7 ± 3.3	5.8 ± 3.5	3.4 ± 3.2	4 ± 3.8
41	4.3 ± 0.5	0.9 ± 0.6	-0.5 ± 0.6	-1.8 ± 0.6	-1.9 ± 0.7
42	3 ± 2.1	-0.2 ± 2.3	-1.2 ± 2.6	-2.5 ± 2.6	-2.6 ± 2.9
43	21.9 ± 3.3	16.2 ± 3.6	14.5 ± 3.7	11.8 ± 4.2	9.9 ± 4.1
44	-8.4 ± 7.7	-9.6 ± 7.9	-9 ± 8.2	-8.6 ± 9.6	-9.3 ± 10.5
45	-7.5 ± 16	-1.8 ± 16.5	2.8 ± 18.2	2.6 ± 19.3	-0.7 ± 20.4
46	37.7 ± 11.4	35.7 ± 12.2	32.1 ± 13.2	29.7 ± 12.7	18.4 ± 13.2
47	-17.9 ± 6.9	-24.7 ± 7.5	-26.5 ± 7.5	-28.3 ± 8.7	-24.7 ± 9.3
48	-25.9 ± 11.2	-27.7 ± 11.5	-28.5 ± 11.8	-25.4 ± 14.2	-23.5 ± 15.6

Table A6. Full fit coefficients for polarized free–free emission in all 48 pixel regions, with associated 1σ errors (in $\mu K\,R^{-1}$).

Pixel	*K* band	*Ka* band	*Q* band	*V* band	*W* band
			Free–free polarization C-C coefficients		
1	-3 ± 5.8	0.8 ± 5.9	-5.4 ± 5.6	-0.7 ± 6.8	1.5 ± 8.3
2	-2.6 ± 5.7	0.3 ± 5.7	1.7 ± 5.4	1.8 ± 6.6	7.9 ± 7.9
3	-10.6 ± 3.5	-0.3 ± 3.7	-0.1 ± 3.6	2.3 ± 4.5	1.6 ± 4.9
4	-1.5 ± 1.2	-0.4 ± 1.3	-0.4 ± 1.2	0 ± 1.5	-1.9 ± 1.8
5	-11.2 ± 2.8	-0.7 ± 2.8	-2.3 ± 2.8	-1.4 ± 3.4	4.5 ± 4.1
6	3.9 ± 2	0.2 ± 2	-0.3 ± 1.9	0.1 ± 2.3	0.8 ± 2.7
7	-4.2 ± 1.6	-1.7 ± 1.7	-0.3 ± 1.5	0.2 ± 2	-0.7 ± 2.4
8	9 ± 3.5	1.4 ± 3.6	-0.4 ± 3.4	-0.5 ± 4.2	-0.5 ± 5
9	1.6 ± 1.6	0.4 ± 1.7	0.4 ± 1.6	0.7 ± 1.9	1.3 ± 2.3
10	-0.3 ± 1.2	1.3 ± 1.2	0.1 ± 1.2	-0.4 ± 1.4	-1.3 ± 1.7
11	0.5 ± 1.1	0.2 ± 1.1	1 ± 1.1	0.2 ± 1.4	-0.3 ± 1.6
12	0.8 ± 1.5	0 ± 1.5	0.7 ± 1.6	-0.8 ± 1.9	-1.9 ± 2.3
13	-1.1 ± 0.8	0 ± 0.8	-0.5 ± 0.8	-0.7 ± 0.9	-0.3 ± 1.1
14	-4.2 ± 0.8	-0.8 ± 0.8	-1.2 ± 0.8	-0.1 ± 0.9	-1.1 ± 1.1
15	-1.5 ± 0.4	-0.4 ± 0.3	-0.2 ± 0.3	0 ± 0.4	0 ± 0.5
16	0.5 ± 0.3	0.1 ± 0.3	0.4 ± 0.4	0 ± 0.4	-0.1 ± 0.5
17	-1 ± 0.5	0.3 ± 0.5	0.2 ± 0.5	0.1 ± 0.6	0.2 ± 0.7
18	0.1 ± 0.9	0.7 ± 1	-0.3 ± 0.9	-0.2 ± 1.1	-0.2 ± 1.4
19	0 ± 0.2	-0.1 ± 0.2	0 ± 0.2	0 ± 0.2	-0.2 ± 0.3
20	-0.6 ± 0.4	0.2 ± 0.5	0 ± 0.4	0 ± 0.5	0.1 ± 0.7
21	-2.1 ± 1.9	1.2 ± 2	-1.1 ± 1.9	-1 ± 2.3	-1.1 ± 2.9
22	-0.8 ± 0.3	-0.2 ± 0.3	-0.3 ± 0.3	0 ± 0.4	0.4 ± 0.5
23	0.2 ± 0.5	0 ± 0.5	-0.1 ± 0.5	-0.2 ± 0.6	-0.2 ± 0.8
24	-3.5 ± 0.8	-1.1 ± 0.8	-1 ± 0.8	-1 ± 1	-0.2 ± 1.2
25	0.9 ± 0.5	0.5 ± 0.5	0.2 ± 0.5	0 ± 0.6	0 ± 0.7
26	0.2 ± 0.2	0.1 ± 0.2	-0.1 ± 0.2	-0.1 ± 0.2	0.1 ± 0.2
27	-0.4 ± 0.2	-0.1 ± 0.2	0 ± 0.2	0 ± 0.3	-0.1 ± 0.3
28	2.6 ± 1.7	1.3 ± 1.7	-0.1 ± 1.6	-0.6 ± 2.1	0.4 ± 2.3
29	-3.6 ± 0.7	-1.8 ± 0.7	-1.4 ± 0.7	0.6 ± 0.9	0.2 ± 1
30	-4.1 ± 1.7	-0.4 ± 1.7	-1.7 ± 1.7	-0.5 ± 2.1	-0.5 ± 2.5
31	-1.4 ± 0.3	0 ± 0.3	-0.2 ± 0.3	0.1 ± 0.3	-0.2 ± 0.4
32	-0.5 ± 0.4	0.2 ± 0.4	-0.2 ± 0.4	0 ± 0.4	0.3 ± 0.5
33	-0.3 ± 0.2	0.1 ± 0.2	0.1 ± 0.2	0.2 ± 0.3	0.3 ± 0.3
34	-0.1 ± 0.1	-0.1 ± 0.1	-0.1 ± 0.1	0 ± 0.2	0.2 ± 0.2
35	-0.2 ± 0.1	-0.1 ± 0.1	-0.1 ± 0.1	0 ± 0.1	0 ± 0.1
36	-1 ± 0.4	-0.3 ± 0.4	-0.3 ± 0.3	-0.2 ± 0.4	0.5 ± 0.5
37	-1 ± 3.4	0.9 ± 3.4	1.5 ± 3.3	0.2 ± 3.8	0.6 ± 4.8
38	-7.3 ± 1.8	-4.1 ± 1.9	-0.8 ± 1.8	0.3 ± 2.2	-0.4 ± 2.7
39	-7.1 ± 2.7	-1.3 ± 2.8	-2.5 ± 2.7	0.2 ± 3.3	-0.3 ± 4
40	3.8 ± 1.1	0.3 ± 1.2	0.4 ± 1	0.3 ± 1.4	0.3 ± 1.5
41	0 ± 0.2	0 ± 0.2	0.1 ± 0.2	-0.1 ± 0.2	0 ± 0.3
42	0.1 ± 0.5	0 ± 0.6	-0.2 ± 0.5	0 ± 0.6	0 ± 0.8
43	-0.9 ± 1.2	0.5 ± 1.1	-1 ± 1	0 ± 1.3	0.2 ± 1.5
44	-7.3 ± 2.2	-2.6 ± 2.3	0.1 ± 2.2	0 ± 2.7	0.5 ± 3.2
45	5 ± 5.9	7.3 ± 6.1	1 ± 6	-0.7 ± 7.3	-1.2 ± 8.5
46	1.2 ± 4.5	1.2 ± 4.8	-2.4 ± 4.6	-1.3 ± 5.6	7.2 ± 6.7
47	2.2 ± 1.6	1.6 ± 1.7	1.8 ± 1.5	-0.5 ± 1.8	1 ± 2.2
48	-0.4 ± 3.4	2.1 ± 3.6	-0.3 ± 3.3	-2.8 ± 4	2 ± 5

This paper has been typeset from a TEX/LATEX file prepared by the author.